Dynamic topography and lithospheric stresses since 400 Ma

Marianne Greff-Lefftz, Boris Robert, Jean Besse, Dominique Frizon de Lamotte, Sophie Vicente de Gouveia

▶ **To cite this version:**

Marianne Greff-Lefftz, Boris Robert, Jean Besse, Dominique Frizon de Lamotte, Sophie Vicente de Gouveia. Dynamic topography and lithospheric stresses since 400 Ma. Geochemistry, Geophysics, Geosystems, 2017, 18, pp.2673-2700. 10.1002/2017GC006936 . insu-03748849

HAL Id: insu-03748849

https://insu.hal.science/insu-03748849

Submitted on 10 Aug 2022

HAL is a multi-disciplinary open access archive for the deposit and dissemination of scientific research documents, whether they are published or not. The documents may come from teaching and research institutions in France or abroad, or from public or private research centers.

L'archive ouverte pluridisciplinaire **HAL**, est destinée au dépôt et à la diffusion de documents scientifiques de niveau recherche, publiés ou non, émanant des établissements d'enseignement et de recherche français ou étrangers, des laboratoires publics ou privés.

Copyright

AGU PUBLICATIONS

Geochemistry, Geophysics, Geosystems

RESEARCH ARTICLE
10.1002/2017GC006936

Dynamic topography and lithospheric stresses since 400 Ma

Marianne Greff-Lefftz[1], Boris Robert[1], Jean Besse[1], Dominique Frizon de Lamotte[2], and Sophie Vicente de Gouveia[1]

[1]Institut de Physique du Globe de Paris-Sorbonne Paris Cité, Université Paris Diderot, UMR CNRS 7154, Paris, France, [2]Département Geosciences et Environnement, Université de Cergy-Pontoise, Cergy-Pontoise, France

Key Points:
- Dynamic topography and surface stresses induced by subducted lithosphere and by long-wavelength upwellings since 400Ma
- The azimuth of the faults plane depends on the direction of the most active part of the ring of subductions
- Mesozoic permanent extensional regime over Africa correlated with the observed direction of the rifts

Supporting Information:
- Supporting Information S1
- Data Set S1
- Data Set S2

Correspondence to:
M. Greff-Lefftz,
greff@ipgp.fr

Citation:
Greff-Lefftz, M., B. Robert, J. Besse, D. Frizon de Lamotte, and S. Vicente de Gouveia (2017), Dynamic topography and lithospheric stresses since 400 Ma, *Geochem. Geophys. Geosyst.*, *18*, 2673–2700, doi:10.1002/2017GC006936.

Received 23 MAR 2017
Accepted 15 JUN 2017
Accepted article online 1 JUL 2017
Published online 24 JUL 2017

© 2017. American Geophysical Union. All Rights Reserved.

Abstract We present a global model of dynamic topography and lithospheric stresses for the last 400 Ma. Our starting point is a simple geodynamic model combining both contributions of subducted lithosphere and long-wavelength upwellings in a reference frame linked to the fixed African plate. A dominant feature of plate tectonics is the quasi permanence of a girdle of subductions around the Pacific Ocean (or its ancestor), which creates large-wavelength positive topography anomaly within the ring they form. The superimposition of the resultant extension with the one induced by the dome leads to a permanent extensional regime over Africa and the future Indian ocean which creates faults with azimuth directions depending on the direction of the most active part of the ring of subductions. We thus obtain fractures with NW-SE azimuth during the period 275–165 Ma parallel to the strike of the subduction zone of the West South American active margin, which appears to be very active during this period. Between 155 and 95 Ma, subduction became more active along the Eastern Australian coast involving a change in the direction of the faults toward an E-W direction, in agreement with the observed fault systems between Africa and India, Antartica and Australia. During the Mesozoic and the Cenozoic, we correlate the permanent extensional regime over Africa and Indian Ocean with the observed rift systems. Finally we emphasize the role of three primary hotspots as local additional contributors to the stress field imposed by our proposed subduction-doming system, which help in the opening of Indian and South Atlantic Oceans.

1. Introduction

Dynamic topography is commonly defined as the vertical motion, at the Earth's surface, induced by mantle convection. It is transient, varying at the time scale of mantle flow. It is not the result of interactions between tectonic plates (such as collisions) and cannot be explained by an isostatic equilibrium of the crust floating on a fluid mantle, nor by nonisostatic flexural effects as well as effects of lithospheric thickness density variations. Present-day residual topography can be estimated by removing the isostatic contribution from the observed topography and all observed topography due to postglacial rebound. Density heterogeneities within the continental lithosphere are not well-known, making its contribution to surface topography difficult to estimate. Consequently, the amplitude of the dynamic topography, still debated (see [*Molnar et al.*, 2015] for precise definition and corrections), seems to be of the order of the kilometer, positive above large-wavelength upwellings and negative above subducted slabs [*Steinberger*, 2016; *Gvirtzman et al.*, 2016; *Hoggard et al.*, 2016].

Dynamic topography can also be reconstructed for the last tens of Myrs from seismic and mantle flow constraints [*Conrad and Gurnis*, 2003; *Liu et al.*, 2008; *Moucha and Forte*, 2011; *Moucha et al.*, 2008; *Spasojević et al.*, 2009; *Wang et al.*, 2015].

At geological time-scale, surface processes can record these episodes of uplift and subsidence of the lithosphere: basins affected by the drift of the continent over the slab [*Mitrovica and Jarvis*, 1985; *Mitrovica et al.*, 1989; *Lithgow-Bertelloni and Gurnis*, 1997; *Liu et al.*, 2011; *Liu*, 2015], sea-level change and observed patterns of flooding [*Gurnis*, 1990; *Gurnis*, 1993; *Gurnis et al.*, 1998; *Spasojević and Gurnis*, 2012; *Guillaume et al.*, 2016], or rifts [see *Braun*, 2010; *Flament et al.*, 2013 for a review].

Mantle circulation also produces stresses within the lithosphere [*Fleitout and Froidevaux*, 1982, 1983; *Ricard et al.*, 1984; *Bai et al.*, 1992; *Lithgow-Bertelloni and Guynn*, 2004; *Ghosh et al.*, 2013], which play an important

role in many geological phenomena. The contribution of these stresses resulting from mantle buoyancy is necessary to explain the amplitude of the orientation of the present-day stresses in many areas especially when they suffer continental deformations [*Ghosh et al*., 2006, 2008] or they undergo oceanic hotspot melt anomalies [*Schiffer and Nielsen*, 2016]. Geological traces of these stresses recorded at Earth's surface, such as the surface directions of rift systems, magnetic anomalies related to oceanic accretion can consequently constrain dynamic processes in the mantle.

In this paper, we present a model of dynamic topography and lithospheric stresses in a reference frame linked to the fixed African plate since 400 Ma. We start with a simple geodynamic model in which we combine contributions from subducted lithosphere [*Ricard et al*., 1993] and from long-wavelength upwellings [*Greff-Lefftz and Besse*, 2012]. Once built this model of temporal variation of the large-scale mantle heterogeneities, we calculate the associated surface topography and lithospheric stresses and compare them with geological observations.

The article is organized as follows. In section 2, we present our theoretical approach with details on our geodynamical model and some simple examples. In section 3, we use our model of temporal evolution of mantle density heterogeneities to compute the dynamic topography and lithospheric stresses in a reference frame linked to the fixed African plate since 400 Ma. Finally we discuss our results and compare them with geological observations and we conclude.

2. Surface Displacements and Viscous Stress Induced by Internal Load

Mantle flow, stresses, and dynamic topography acting at the base of the lithosphere are usually calculated assuming a viscous or elastic lithosphere and a viscous Newtonian mantle [*Ricard et al*., 1984; *Steinberger et al*., 2001]. Here we assume a viscoelastic model for both lithosphere and mantle [*Peltier*, 1974] and we compute the viscoelasto-gravitational deformations, that is to say the radial and tangential displacement at Earth's surface and within the mantle as well as the stresses. The Maxwell's viscoelastic body, on the geological time scales which interest us here, is equivalent to the Newtonian viscous fluid. Nevertheless, such a rheology would allow us, if necessary, to introduce a lithosphere or an elastic crust. We first present our theoretical approach and then illustrate it with characteristic examples.

2.1. Surface Displacements

To study the viscoelastic deformations of a prestressed planet, we must solve the equations of dynamics (conservation of mass and momentum) coupled with the Poisson equation and a state equation linking stresses to strains (rheological law). We suppose that the incompressible radially stratified mantle is a linear viscoelastic body following the Maxwell's law. The Laplace transform of the stresses/strains law for a Maxwell body is the Hooke's law, with the shear modulus μ^i in each layer i of the mantle dependent on the frequency s:

$$\mu^i(s)=\mu^i_{el}\frac{s}{s+\frac{\mu^i_{el}}{\nu^i}} \tag{1}$$

where ν^i is the viscosity and μ^i_{el} is the elastic shear modulus of the layer i. Because the viscoelastic equations and the boundary conditions in Laplace domain are the same than those for an elastic body with the same geometry, we may use the correspondence principle [*Peltier*, 1974]: we solve the elastic problem for different frequencies in order to build the viscoelastic solutions.

In our approach, we do not take into account lateral viscosity variations. We use a five layered Earth model, with a 100 km thick viscoelastic lithosphere, a viscoelastic upper and lower mantle, an inviscid fluid core, and a viscoelastic inner core. We assume that the lithosphere and the whole mantle have the same density ($\rho^m=4455\,\mathrm{kg/m^3}$), and we set the density of the fluid core to $10,900\,\mathrm{kg/m^3}$ and of the inner core to $12894\,\mathrm{kg/m^3}$.

The viscoelasto-gravitational equations are written using a Lagrangian formulation and the spheroidal displacement vector field $\vec{u}$ is expanded in spheroidal vector of degree n and order m, with the use of two radial function $y_{1n}(r)$ and $y_{3n}(r)$ [*Alterman et al*., 1959].

$$\vec{u}=\sum_{n=1}^{\infty}\sum_{m=0}^{n} y_{1n}(r)Y_n^m(\theta,\varphi)\frac{\vec{r}}{r}+ry_{3n}(r)\vec{\nabla}Y_n^m(\theta,\varphi) \tag{2}$$

where $Y_n^m(\theta,\varphi)$ are the spherical harmonics of degree n and order m, θ is the colatitude, and φ is the longitude. When the excitation source is an internal load located at the radius r_o, the solutions at Earth's surface ($r=a$), $y_{1n}(a)$ and $y_{3n}(a)$ are described in *Greff-Lefftz et al.* [2010] with the use of viscoelastic degree n Love numbers, noted $h'_n(s,r_o)$ for the radial displacement or $l'_n(s,r_o)$ for the tangential displacement. For the degree n coefficient of the spherical harmonics expansion of the internal loading potential (S^{int}), the degree n radial and tangential displacements may be written:

$$y_{1n}(a,s)=h'_n(s,r_o)\frac{S_n^{int}(s,r_o)}{g_o} \tag{3}$$

$$y_{3n}(a,s)=l'_n(s,r_o)\frac{S_n^{int}(s,r_o)}{g_o} \tag{4}$$

where g_o is the surface gravity and

$$h'_n(s,r_o)=h'^{el}_n(r_o)+\sum_{j=1}^{M}\frac{h_{nj}(r_o)\tau_{nj}}{1+s\tau_{nj}} \tag{5}$$

$$l'_n(s,r_o)=l'^{el}_n(r_o)+\frac{l_{n0}(r_o)}{s}+\sum_{j=1}^{M}\frac{l_{nj}(r_o)\tau_{nj}}{1+s\tau_{nj}} \tag{6}$$

where $h'^{el}_n(r_o)$ and $l'^{el}_n(r_o)$ are the elastic Love numbers, h_{nj} and l_{nj} are the residues associated with the τ_{nj}, the M viscoelastic relaxation times of degree n [*Peltier*, 1974].

At the time scale of the mantle convection, $s\tau_{nj}\ll 1$ and consequently:

$$h'^{f}_n(r_o)\simeq h'^{e}_n(r_o)+\sum_{j=1}^{M}h_{nj}(r_o)\tau_{nj} \tag{7}$$

$$l'^{f}_n(s,r_o)\simeq l'^{e}_n(r_o)+\frac{l_{n0}(r_o)}{s}+\sum_{j=1}^{M}l_{nj}(r_o)\tau_{nj} \tag{8}$$

where the superscript ^{f} denotes the quasi-fluid limit.

We note $S_n^{int,f}(r_o)=S_n^{int}(0,r_o)$ is the degree n coefficient of the spherical harmonics expansion of the quasi-fluid internal loading potential.

We set the viscosity of the lithosphere to 1.1×10^{22} Pa.s, the viscosity of the upper mantle to 10^{21} Pa.s, and the viscosity of the lower mantle to 4×10^{22} Pa.s. [*Ricard et al.*, 1993]. For this model, we plot, in Figure 1a, $h'^{f}_n(r_o)$ is the viscous kernel of the radial displacement as a function of r_o for the degree 1 up to 12. This kernel is always negative and consequently a positive mass anomaly in the mantle (such as cold slab) will induce a negative topography. Note that the surface topography kernel decreases with depth and increases with the degree n: topography will be consequently strongly affected by local mass anomalies in the upper part of the mantle. The degree 0 loading Love number $h'^{f}_0(r_o)$ is exactly equal to zero because we assume an incompressible Earth's model and consequently the topography averages to zero when integrated over the surface of the Earth.

Note that in this study, we define the dynamic topography as the surface vertical displacement induced by the mantle density heterogeneities, whereas in most of the previous studies the dynamic topography results from a balance between radial traction at the base of the lithosphere and the opposed buoyancy force [*Bai et al.*, 1992]. Our approach allows variable stresses throughout the lithosphere, variation of the lithospheric thickness and includes the effects of self-gravitation.

2.2. Viscous Stresses

Because of the correspondence principle [*Peltier*, 1974], we can compute the six components of the stress tensor σ_{ij}, in the Laplace domain from the Hooke law. At the surface, in absence of acting tangential

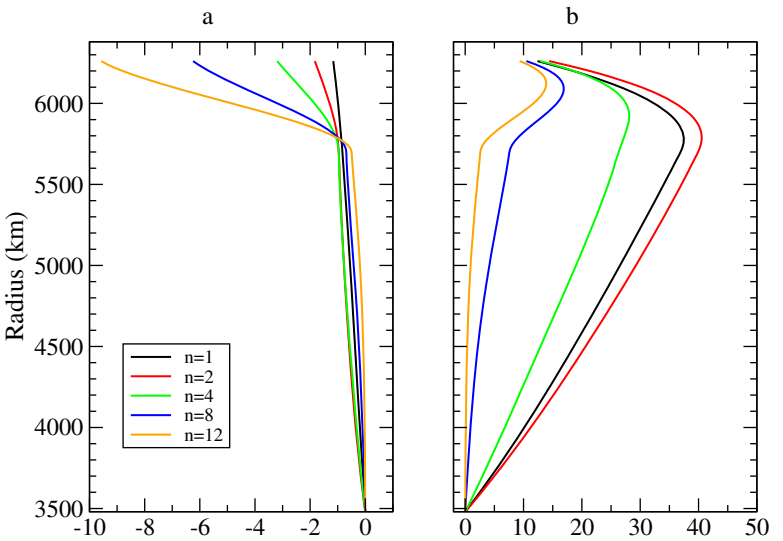

Figure 1. Viscous kernels of the surface displacement as a function of the radius r_o where is located the internal load, for different degree n: (left) Love number $h_n^{tf}(r_o)$ for the radial displacement; (right) Love number $l_{n0}(r_o)$ in 1/kyr for the tangential displacement.

traction, pressure, and surface load, the radial traction has to be equal to zero; consequently σ_{rr}, $\sigma_{r\theta}$, and $\sigma_{r\varphi}$ are equal to zero.

In spherical coordinates (r, θ, φ), we have

$$\sigma_{rr} = \lambda \mathrm{div}\vec{u} + 2\mu \frac{\partial u_r}{\partial r} \tag{9}$$

and consequently, at the surface, for an incompressible body:

$$\lambda \mathrm{div}\vec{u} = -2\mu \frac{\partial u_r}{\partial r} \tag{10}$$

The three components $\sigma_{\theta\theta}$, $\sigma_{\varphi\varphi}$, and $\sigma_{\theta\varphi}$ may be computed from the displacements [e.g., *Dahlen and Tromp*, 1998]:

$$\sigma_{\theta\theta} = \lambda \mathrm{div}\vec{u} + 2\mu \left[\frac{1}{r}\frac{\partial u_\theta}{\partial \theta} + \frac{u_r}{r}\right] \tag{11}$$

$$\sigma_{\varphi\varphi} = \lambda \mathrm{div}\vec{u} + 2\mu \left[\frac{1}{r\sin\theta}\frac{\partial u_\varphi}{\partial \varphi} + \frac{u_r}{r} + \cot\theta \frac{u_\theta}{r}\right] \tag{12}$$

$$\sigma_{\theta\varphi} = \mu \left[\frac{1}{r\sin\theta}\frac{\partial u_\theta}{\partial \varphi} + \frac{1}{r}\frac{\partial u_\varphi}{\partial \theta} - \cot\theta \frac{u_\varphi}{r}\right] \tag{13}$$

Or, by replacing u_r, u_θ, and u_φ by their expressions as a function of y_{1n} and y_{3n} (2):

$$\sigma_{\theta\theta} = 2\frac{\mu^1(s)}{a}\sum_{n=1}^{\infty}\sum_{m=0}^{n}\left[3y_{1n}(a)Y_n^m(\theta,\varphi) + y_{3n}(a)\left(-n(n+1)Y_n^m(\theta,\varphi) + \frac{\partial^2}{\partial\theta^2}Y_n^m(\theta,\varphi)\right)\right] \tag{14}$$

$$\sigma_{\varphi\varphi} = 2\frac{\mu^1(s)}{a}\sum_{n=1}^{\infty}\sum_{m=0}^{n}\left[3y_{1n}(a)Y_n^m(\theta,\varphi) - y_{3n}(a)\left(2n(n+1)Y_n^m(\theta,\varphi) + \frac{\partial^2}{\partial\theta^2}Y_n^m(\theta,\varphi)\right)\right] \tag{15}$$

$$\sigma_{\theta\varphi} = 2\frac{\mu^1(s)}{a}\frac{1}{\sin\theta}\sum_{n=1}^{\infty}\sum_{m=0}^{n}y_{3n}(a)\left[\frac{\partial}{\partial\theta}\frac{\partial}{\partial\varphi}Y_n^m(\theta,\varphi) - \cot\theta\frac{\partial}{\partial\varphi}Y_n^m(\theta,\varphi)\right] \tag{16}$$

where $\mu^1(s)$ is the viscoelastic rigidity of the lithosphere.

At geological time scale, we have:

$$\lim_{s\to 0}\mu^1(s)l_n^{lf}(s,r_o)=v^1 l_{n0}(r_o); \qquad \text{and} \qquad \lim_{s\to 0}\mu^1(s)h_n^{lf}(r_o)=0 \tag{17}$$

and consequently:

$$\sigma^f_{\theta\theta}=2v^1\sum_{n=1}^{\infty}\sum_{m=0}^{n} l_{n0}(r_o)\frac{S_n^{int,f}(r_o)}{g_o a}\left[-n(n+1)Y_n^m(\theta,\varphi)+\frac{\partial^2}{\partial\theta^2}Y_n^m(\theta,\varphi)\right] \tag{18}$$

$$\sigma^f_{\varphi\varphi}=-2v^1\sum_{n=1}^{\infty}\sum_{m=0}^{n} l_{n0}(r_o)\frac{S_n^{int,f}(r_o)}{g_o a}\left[(2n(n+1)Y_n^m(\theta,\varphi)+\frac{\partial^2}{\partial\theta^2}Y_n^m(\theta,\varphi)\right] \tag{19}$$

$$\sigma^f_{\theta\varphi}=2v^1\sum_{n=1}^{\infty}\sum_{m=0}^{n} l_{n0}(r_o)\frac{S_n^{int,f}(r_o)}{g_o a}\frac{1}{\sin\theta}\left[\frac{\partial}{\partial\theta}\frac{\partial}{\partial\varphi}Y_n^m(\theta,\varphi)-\cot\theta\frac{\partial}{\partial\varphi}Y_n^m(\theta,\varphi)\right] \tag{20}$$

the stresses are the Newtonian viscous stresses and are proportional to the viscosity of the lithosphere v^1.

The viscous Love number $l_{n0}(r_o)$ is plotted on Figure 1b in 1/kyr for degree n ranging from 1 to 12.

Finally, at Earth's surface, the viscous stress tensor induced by internal load is:

$$\sigma=\begin{pmatrix}0 & 0 & 0\\ 0 & \sigma^f_{\theta\theta} & \sigma^f_{\theta\varphi}\\ 0 & \sigma^f_{\theta\varphi} & \sigma^f_{\varphi\varphi}\end{pmatrix} \tag{21}$$

We now compute the maximal shear stress and the dip p and azimuth A of the associated fault plane whose normal is, in the spherical basis $(\vec{e}_r,\vec{e}_\theta,\vec{e}_\varphi)$:

$$\cos p\vec{e}_r+\sin A\ \sin p\vec{e}_\theta+\cos A\ \sin p\vec{e}_\varphi \tag{22}$$

To do that, we have to work in the reference frame of the Principal Stresses Axis. We first compute the eigenvalues $(\sigma_1>\sigma_2>\sigma_3)$ and the eigenvectors associated with our viscous stress tensor, and then use Mohr's Circle, a tool to visualize relationships between normal and shear stresses to estimate the maximal stress $\tau_{\max}=\frac{\sigma_1-\sigma_3}{2}$, the associated normal stress $\frac{\sigma_1+\sigma_3}{2}$ as well as the azimuth of the fault plane (Appendix A).

2.3. Four Examples

In this section, we illustrate our theoretical approach with four simple examples corresponding to the four characteristic elements of the large-scale mantle convection.

2.3.1. A Dome in the Lower Mantle

We assume a large region at the bottom of the mantle, stable with time, which accounts for a thermochemical dome. This dome is associated with a geoid high and is consequently modeled as a region with a negative mass anomaly with respect to the mantle. We arbitrarily fixed its density contrast with respect to the surrounding mantle to -50 kg/m^3 although these densities are still debated. The mass anomalies associated with such a dome are modeled as one hemisphere with a radius α and a height h, centered at the coordinates $(-15°\text{S}, 30°\text{E})$. The width α of the dome is fixed to 55° and from the present-day tomography we set $h=600$ km. Using our previous formalism, we compute the surface topography (Figure 2a), the normal stress (Figure 2b) and the shear stresses (Figure 2c) induced by such mantle mass anomalies. At the center of the dome, the amplitude of the topography is about 250 m and the maximal shear stress about a few MPa and the normal stress is extensive ($\sigma>0$). Above the domes, the fractures are radial.

2.3.2. A Plume Beneath the Lithosphere

We simply model a plume as a spherical head with a radius of about 250 km and a trailing conduit whose volume is negligible. The density contrast is set to $-30\,\text{kg/m}^3$. The center of the spherical head is such that the top of the plume head is just at the base of the lithosphere. We plot in Figure 3 the associated surface deformations: above the plume, the topography (Figure 3a) is about 750 m, the normal stress (Figure 3b) is extensive and the shear stresses (Figure 3c) are about 60 MPa. Similarly to the domes, the fractures are radial with respect to the center of the plume. Note that this extension results only from mantle buoyancy and appears at the surface before the first traces of volcanism.

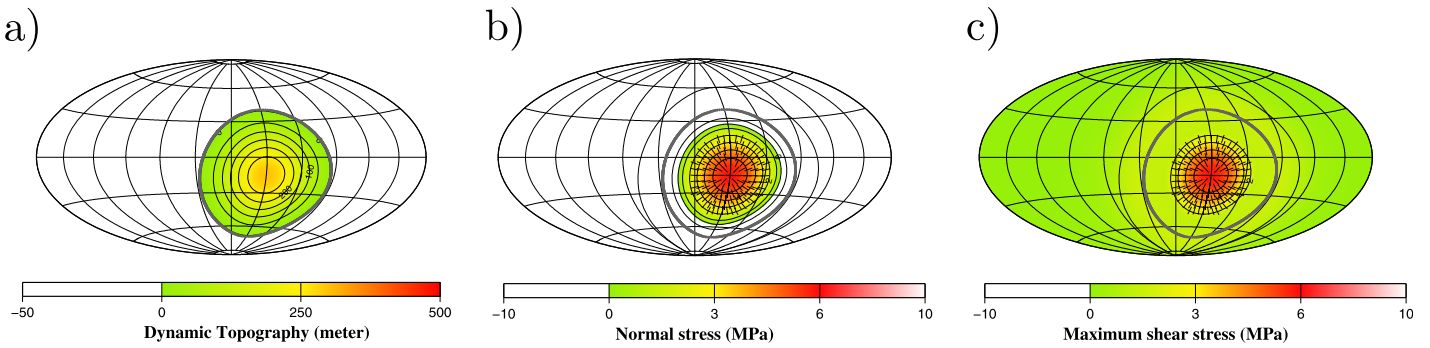

Figure 2. Upwelling dome in the lower mantle. (left) Dynamic topography in meters; (middle) normal stress in MPa; and (right) maximal shear stress in MPa (Hammer projection). The black line segments are the fault planes.

2.3.3. A Downwelling Plate Within the Mantle

We assume an equatorial convergence zone in which a plate starts to sink vertically within the mantle at $t = 0$. We use a model proposed by *Ricard et al.* [1993]: when the slab is in the upper-mantle, its downward velocity is the surface convergence velocity (in this example fixed to 8 cm/yr). The slab reaches the 670 km depth discontinuity after a time T_1 about 8 Myrs. In the lower mantle, the velocity of the slab is assumed to decrease by a factor 4 whereas its size (the thickness) increases by the same factor 4, for a viscosity ratio between upper and lower mantle about 40. In this example, the characteristic time needed for a plate to sink through the whole mantle is $T_2 \simeq 120$ Myrs. The density contrast with respect to the PREM average densities throughout the mantle is set to 80 kg/m^3. We compute the surface topography (Figure 4b), the normal stress (Figure 4c), and the maximal shear stress (Figure 4d) induced by such mantle mass anomalies at $t = 150$ Myrs, i.e., when there are cold mass anomalies from the surface to the core-mantle boundary ($t > T_2$, Figure 4a). Above the subduction zone, the amplitude of the topography is about -1800 m, τ_{max} is about 60 MPa and the normal stress is compressive ($\sigma < 0$). The fractures are aligned with the subduction zone just above it and concentric with respect to the subduction zone far from it when the normal stress is extensive.

2.3.4. A Downwelling Plates Within the Mantle Along a Ring of Subduction

Because the peri-Pacific subduction (or its ancestor) is a quite permanent feature of Earth's history at least since 400 Ma, we now assume stable subductions located on a small circle centered at 5°N, 50°E with a radius about 80° (grey circle on Figure 5). The surface velocity is constant (in this example, fixed to 8 cm/yr) and slabs start to sink in the mantle at $t = 0$. The surface topography, the normal and maximal shear stresses as well as the azimuth of the fault plane are plotted on Figure 5, for a time $t = 150$ Myr when the

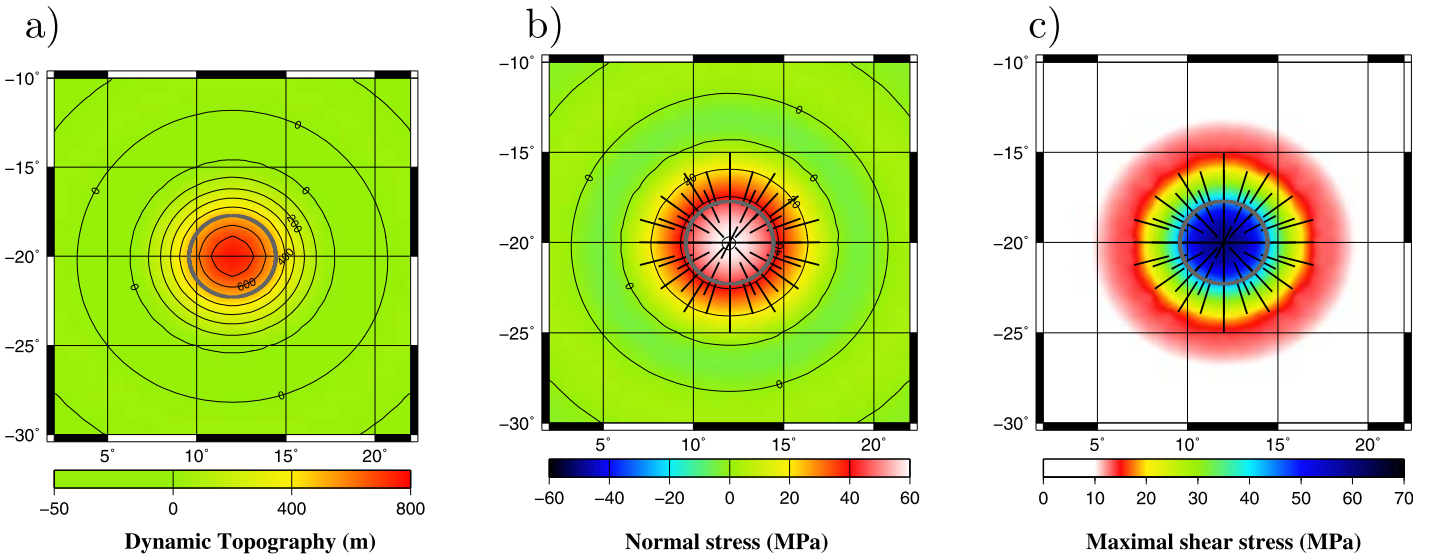

Figure 3. Plume beneath the lithosphere. (left) Dynamic topography in meters; (middle) normal stress in MPa; and (right) maximal shear stress in MPa (linear projection). The black line segments are the fault planes.

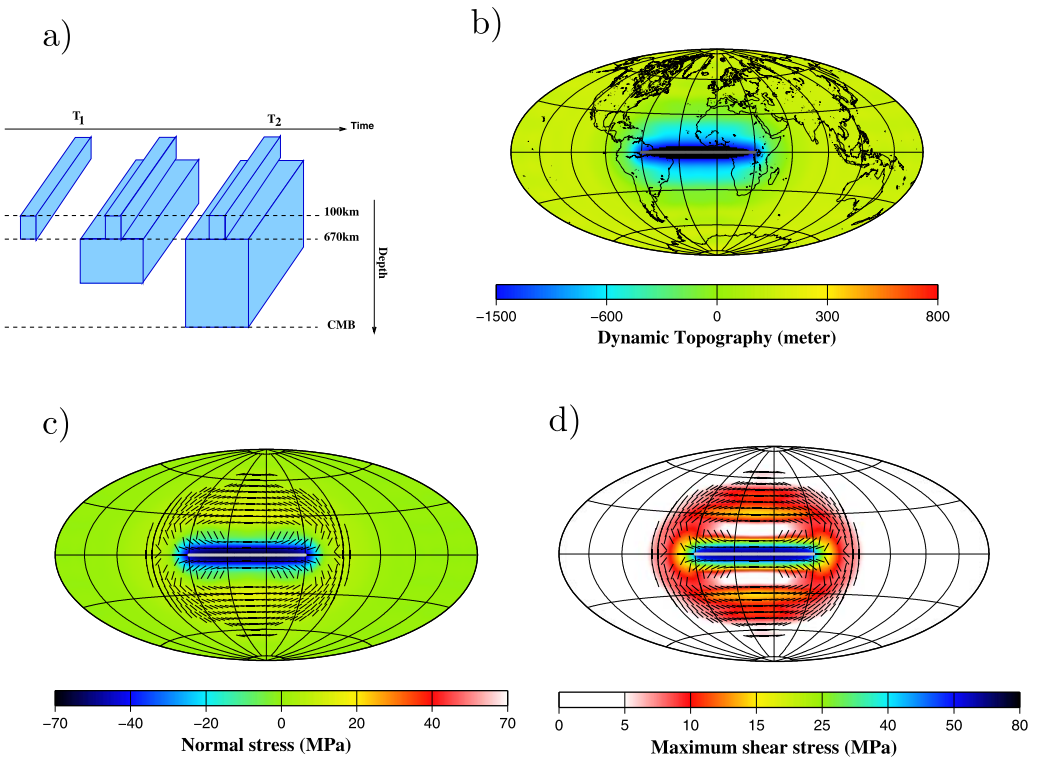

Figure 4. Downwelling plate within the mantle along a subduction zone. (a) Model of plate in the mantle as a function of the depth, (b) dynamic topography in meters, (c) normal stress in MPa, and (d) maximal shear stress in MPa (Hammer projection). The black line segments are the fault planes.

plates have sunken through the whole mantle. Fractures are aligned with the subduction zone just above it and concentric in the middle of the small circle. Above the subduction zone, the topography is about −1700 m, the maximal shear stress τ_{max} is about 70 MPa and the associated normal stress is compressive ($\sigma < 0$), whereas within the circle of subduction, the topography is about 750 m, τ_{max} is about 15 MPa and the associated normal stress is extensive ($\sigma > 0$).

Some [e.g., *Becker and Boschi*, 2002; *Ren et al.*, 2007] but not all [*Fukao et al.*, 2001] tomographic images inferred from seismology suggest that the density heterogeneities associated with subducted plates may reach the Core-Mantle Boundary (CMB). We thus investigate the influence of the depth down to which the subducted peri-Pacific plates present a significant density contrast with respect to the surrounding mantle. We plot in Figure 5d the amplitude of the topography, the maximal shear stress, and the compressive normal stress above the subduction zone (solid line) as well as the positive topography and extensive normal stress in the middle of the circle of subduction (dashed line) as a function of this depth from 1000 km down to the CMB. Although the topography and stress kernels are sensitive to masses in the upper part of the mantle, there is a significant contribution of the slabs in the lower mantle: the amplitude of both the dynamic topography and the surface stresses can vary by a factor two following the value of the depth down to which the subducted plates sink into the mantle. This is because in our approach, we assume that the slabs are folded or thickened by a factor of 4 at the 670 km discontinuity and consequently we have large sheets of cold material in the lower mantle. Nevertheless, slabs deeper than 2100 km do not perturb the surface signals. This range of amplitudes has to be kept in mind in the rest of this study.

3. Dynamic Topography and Lithospheric Stresses in a Reference Linked to the Fixed African Plate Since 400 Ma

In this section, we start from a simple geodynamic model [*Greff-Lefftz and Besse*, 2012]. This model that simply combines contributions from subducted lithosphere and from long-wavelength upwellings is detailed in Appendix B. Briefly, it was constructed following the steps summarized below.

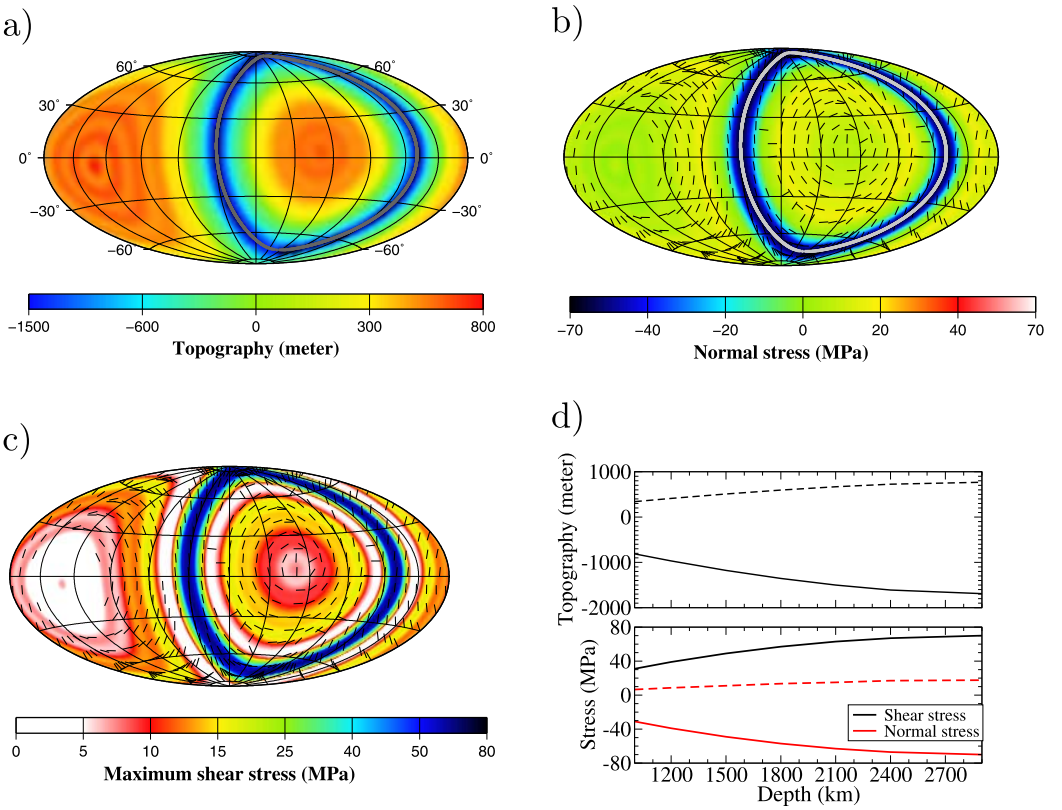

Figure 5. Ring of subduction. (a) Dynamic topography in meters, (b) normal stress in MPa, (c) maximal shear stress in MPa (Hammer projection), (d) amplitude of the topography, the maximal shear stress, and the compressive normal stress above the subduction zone (solid line) as well as the positive topography and extensive normal stress in the middle of the circle of subduction (dashed line) as a function of the depth down to which the subducted plate is sinking into the mantle.

1. We first investigated plate motions during the last 400 million years from geological, paleomagnetic, and subduction-related calc-alkaline volcanism data. Then, assuming that plates sink down to the core-mantle boundary, we modeled the temporal evolution of mantle density heterogeneities associated with subductions. In a previous paper [*Greff-Lefftz and Besse*, 2012], we used 14 interpolated plate stages between 410 and 130 Ma. Here, we build mantle density heterogeneities models using stages lasting 10 Myr. For the period between 410 and 200 Ma, we keep our previous plates motions. For the period between 200 and 120 Ma, we start from a compilation of plates motions by *Seton et al.* [2012] in which we modify the position of the Neo-Tethys subduction to take into account the Mongol-Okhotsk ocean situated between the Amuria North China block and Silesia [*Cogné et al.*, 2005].
2. Then, from intraplate volcanism, we identified two broad areas on Earth's surface above the two antipodal domes in the deep mantle, large regions in which material is thermally or compositionally less dense than the surrounding mantle. The domes are modeled as two hemispheres with variable width, fixed height ($h = 600$ km), and fixed density contrast with respect to the surrounding mantle ($-50\,\mathrm{kg/m^3}$).

The position of the subduction zones are plotted as white dots lines on Figure 6, whereas the location of the antipodal domes are figured as grey small circles. See Appendix B for details of this geodynamic model.

For this model of temporal variation of the large-scale mantle heterogeneities, we calculate the associated surface dynamic topography and lithospheric stresses in the geological past, using the theoretical approach described in the previous section.

3.1. Dynamic Topography

In Figure 6, we show the dynamic topography since 280 Ma. For the different periods of time, we find, on one hand, a large-scale positive dynamic topography above the domes, a usual explanation for the present-day superswells observed at Earth's surface [*Lithgow-Bertelloni and Silver*, 1998; *Behn et al.*, 2004], and on the

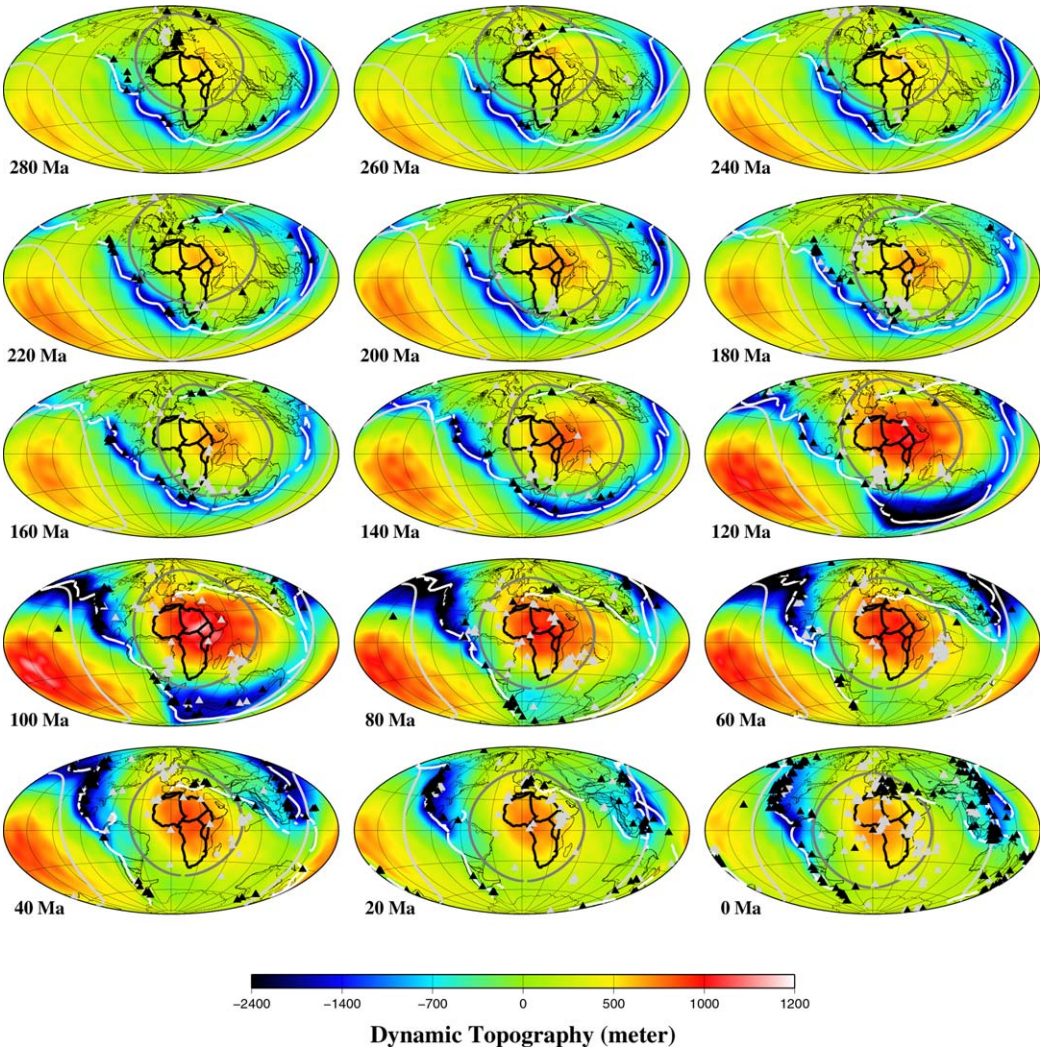

Figure 6. Dynamic topography at different periods of time (in meters) in the fixed African plate reference frame (Hammer projection). The grey triangles denote intraplate volcanism and black triangles are for the subduction volcanism; the grey small circles feature the position of the domes at the bottom of the mantle and the white dots lines the subduction zones (modified from [*Greff-Lefftz and Besse*, 2012] and [*Seton et al*., 2012]).

other hand, we obtain negative topography above the subduction zones and positive at the center of the peri-Pacific ring of subduction.

Let us first discuss the global signature of our predicted dynamic topography and then some regional results.

3.1.1. Degree-Power Spectrum of the Dynamic Topography

We compute and plot in Figure 7a the degree-power spectrum $S(n, t)$ of our modeled dynamic topography as a function of time t and of the spherical harmonics degree n.

$$\sum_{n=1}^{12}[S(n,t)]^2=\frac{1}{4\pi}\int_0^{2\pi}\int_0^{\pi}[u_r(a,\theta,\varphi,t)]^2\sin\theta d\theta d\varphi \tag{23}$$

Our predicted dynamic topography shows large-wavelength structures (we do not take into account the shallow, short-wavelength mantle density anomalies which would create significant power spectra at high degrees). The dominant degree is the degree $n = 2$. There is also a significant degree-one spectrum with an amplitude of about a few hundred meters, which may be related to a geocenter motion at geological time-scale [*Greff-Lefftz et al*., 2010]. We plot in Figure 7b, the degree-power spectrum at the present-day (in grey) and 100 Ma ago (in black). We find that the amplitude of the dynamic topography was larger 100 Ma ago

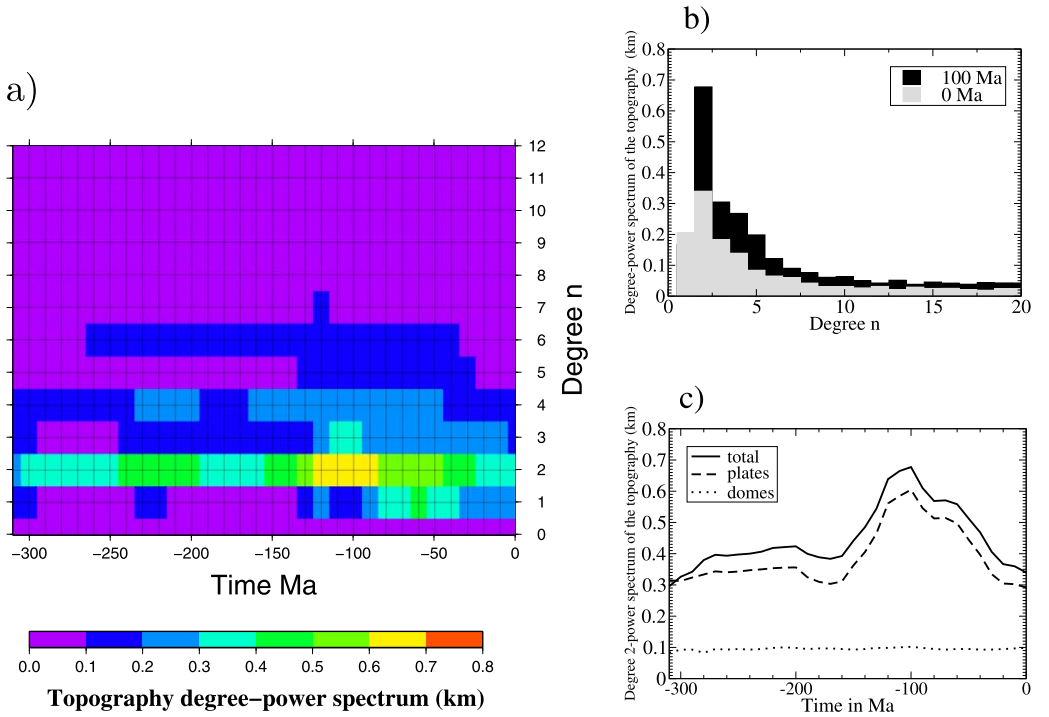

Figure 7. Dynamic topography degree-power spectrum: (a) as a function of degree and time, (b) as a function of degree for present-day and 100 Ma ago, and (c) as a function of time for degree 2.

than currently: this may be explained by the larger plate-velocities at the subduction zones during the Early Cretaceous Period, and consequently by the larger associated mantle density heterogeneities at this time (Appendix B, Figure B2). The present-day power-spectrum shows a large degree 2 as usually predicted in different models of dynamic topography [*Flament et al*., 2013], but that does not exist in the models derived from topography observations [see *Hoggard et al*., 2016, Figure 5b]. However, the continental dynamic topography derived by *Hoggard et al*. [2016] is based on a questionable hypothesis: in the continents, they assumed a constant gravity to topography ratio for these long wavelengths, whereas at the longest wavelengths, it is well-known that free-air anomaly is sensitive to mantle mass anomalies within the whole mantle and the gravity kernels change sign with depth [*Richards and Hager*, 1984] while the topography kernel remains negative [see *Yang and Gurnis*, 2016; *Colli et al*., 2016 for a detailed discussion].

To understand the origin of our predicted degree 2 signal, we plot in Figure 7c, the temporal evolution of the degree-2 power spectrum (in solid line) and separate it into two contributions: the one induced by the subducted plates alone (dashed line) and the one due to the domes alone (dotted line). As shown in the examples 2.3.1 and 2.3.3 where a dome involves a topography of about 250 m at its apex and a ring of subduction a topography about 750 m in the middle of the ring (for a plate velocity about 8 cm/yr), we find that there is a factor ranging from 3 to 6 between the amplitudes of the degree 2 power spectrum induced by the subducted plates and the one induced by the two antipodal domes. Most of the degree 2 dynamic topography is induced by the plates sinking within the mantle and consequently is related to the degree 2 distribution of the subduction zones, i.e., to the peri-Pacific girdle of subduction zones. In our model, we certainly overestimate the degree 2 mantle density heterogeneities within the bottom of the lower mantle, assuming that all plates sink down to the CMB. Considering shear heating and compressibility would also reduce degree 2 mantle density heterogeneities.

3.1.2. Regional Dynamic Topography

The temporal evolution of the dynamic topography (subsidence and uplift of continents) can control regional sea-level [e.g., *Conrad and Husson*, 2009; *Conrad*, 2013; *Guillaume et al*., 2016]. A consequence is that continental flooding can be influenced by the movement of continents over large-scale mantle mass anomalies, with, for example, slabs creating large topographic depressions [*Mitrovica and Jarvis*, 1985].

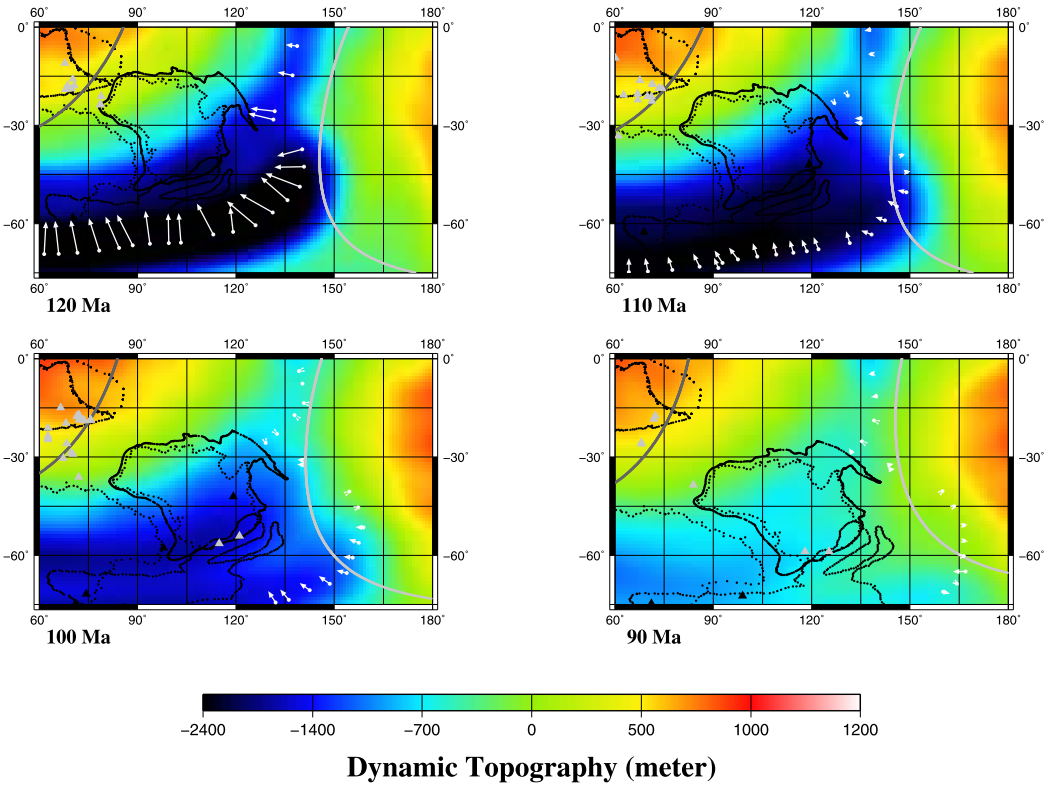

Figure 8. Dynamic topography, in meters, over in Australia during the Cretaceous (linear projection): the white arrows denote the convergence rate at the active margin. The grey triangles feature the intraplate volcanism.

Geological fingerprints at the surface of such mechanism have been largely investigated [see *Flament et al.*, 2013 for a review]:

1. Mantle circulation models driven by subduction explaining floodings in the Middle Ordovician, Late Permian, and Early Cretaceous (periods of flooding during eustatic heights) [*Gurnis*, 1993].
2. Extensive Cretaceous flooding following by the uplift of the Western Interior Seaway [*Mitrovica et al.*, 1989; *Liu et al.*, 2008; *Spasojević et al.*, 2009; *Liu*, 2015], Cenozoic uplift and subsidence of North America, Australia [*Heine et al.*, 2010], Indonesia [*Lithgow-Bertelloni and Gurnis*, 1997], and South America [*Flament et al.*, 2015].
3. Anomalous Cretaceous vertical motions of Australia induced by the drift of the continent over a slab associated with Pacific subduction [*Gurnis et al.*, 1998].

To illustrate this last point with our model, we plot on Figure 8 the dynamic topography during Cretaceous times for Australia: we obtain a large depression over the South-East region of Australia between 120 and 110 Ma, which can be correlated with the period of maximum flooding [*Struckmeyer and Brown*, 1990], followed by an uplift between 110 and 90 Ma. This is consistent with the gradual removal of Australia from the subducted slab area [*Gurnis*, 1993]. The rate of the uplift from 20 up to 50 m/Myr seems to be a plausible value although difficult to compare with observations of tectonic subsidence [*Matthews et al.*, 2011; *Czarnota et al.*, 2014; *Rudge et al.*, 2015].

The topographic evolution in the northwest of America is marked by a large depression induced by slabs sinking into the mantle since the Mesozoic from 120 to 90 Ma (Figures 9a and 9b). To quantify it, we plot on Figure 9c the temporal evolution of the uplift at the red point (Colorado): the amplitude of our topographic low increases from −800 m up to −1500 m and then remains stable until 40 Ma, age from which an uplift appears with a decrease in the amplitude of the depression (Figure 9c). We obtain a present-day topographic low (∼−1000 m) as opposed to the high inferred in other models and in residual topography. This topographic low results from the combination of a significant plate convergence rate at the subduction

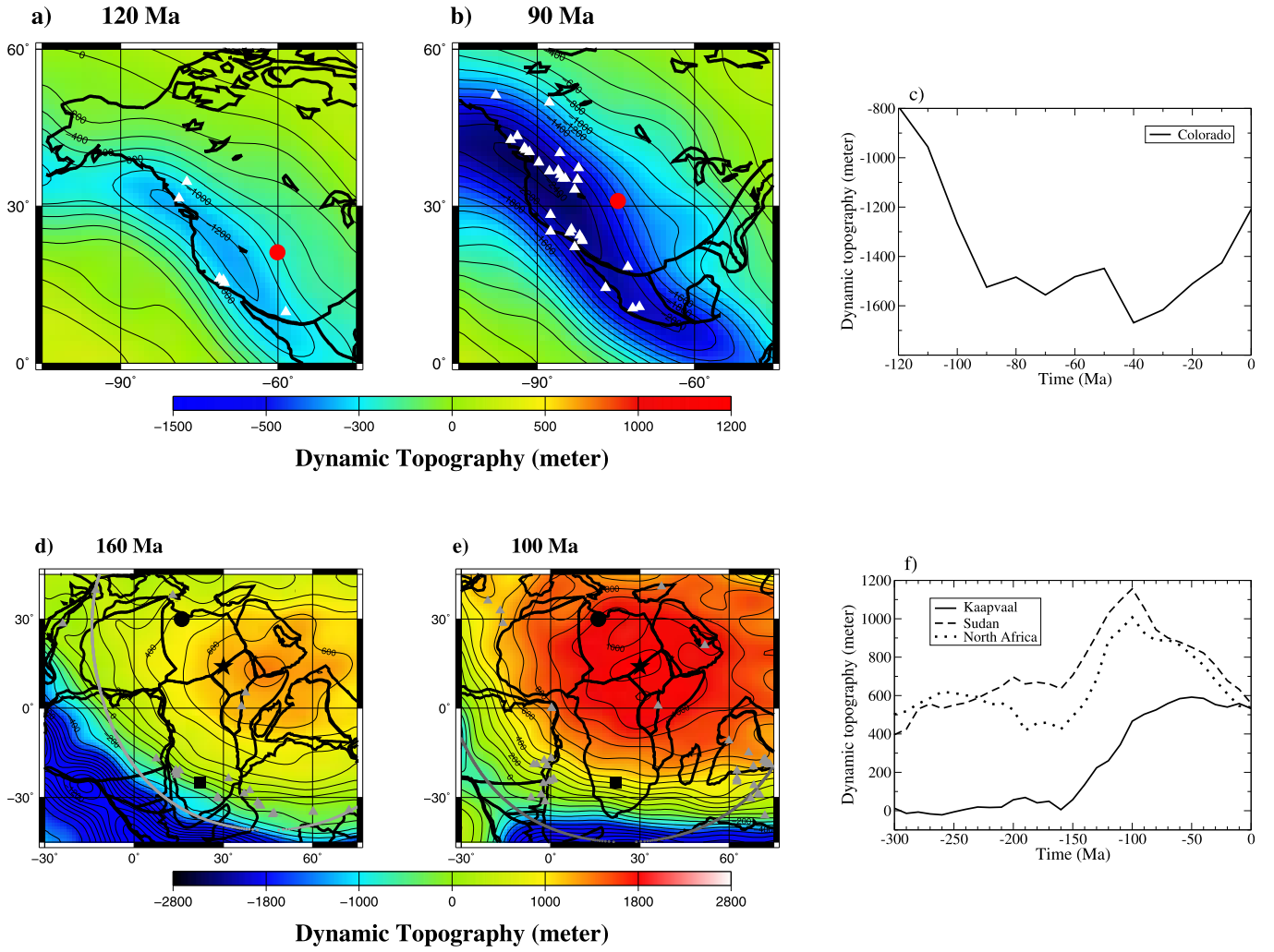

Figure 9. Dynamic topography over North America (a) 120 Ma ago and (b) 90 Ma ago and extension over Africa (d) 160 Ma ago and (e)100 Ma ago. The red filled circle, black filled square, black star, and black filled circle are the points over the Colorado, Kaapvaal craton, Sudan, and North Africa discussed in the text. The grey small circle features the position of the African dome at the bottom of the mantle, the white triangles the subduction volcanism, and the grey triangles the intraplate volcanism (linear projection). Temporal evolution of the dynamic topography at these points (c and f).

zone until 20 Ma with the migration of the active continental margin leading to a more or less vertical quantity of masses sinking within the mantle with effective dip angle always greater than 50° [see *Lithgow-Bertelloni and Richards*, 1998, Figure 5]. Our model, only valid for long-wavelength mantle density heterogeneities, does not include returning passive upwelling from downwelling below the eastern part of America nor involve flat slab. As a matter of fact, recent models using present-day seismic images to infer past mantle mass anomalies with thermal diffusion [see *Liu*, 2015, for a review] show that the Western Interior Seaway created during the Late Cretaceous by a topographic low induced by the subduction of the Farallon slab with a quasi-horizontal dip angle and that, the removal of the flat slab was responsible for the rebound of the surface, explaining the present-day uplift [*Liu and Gurnis*, 2010]. The precursory deformations before the appearance of the Yellowstone hotspot at the surface, 16 Ma ago [*Courtillot et al*., 2003] or any other upwelling in the mantle may also contribute to the observed uplift [*Moucha et al*., 2009].

We now focus on the topographic evolution of Africa in more detail.

The position of the African dome, constrained by the intraplate volcanism remains close to the paleomagnetic equator in our fixed African plate reference frame (see Appendix B and Figure B3). Its associated topography is consequently superimposed to the one associated with the peri-Pacific subduction, leading to a permanent extensional regime over Africa. Note that the westward drift of the African dome during the

Cenozoic, in our reference frame linked to the fixed African plate, implies a westward migration of the topographic high. *Braun et al*. [2014] have already explained this tilt (in a mantle reference frame) by the drift of the continent over a fixed mantle upwelling, and constrained it with observations of pulses of erosion.

We present a zoom onto this region at 160 and 100 Ma (Figures 9d and 9e), showing that the amplitude of topography increased during the Early Cretaceous. To quantify this extension, we compute the vertical displacement at the point with latitude θ=14°N and longitude φ=30° (black star in the middle of the present Sudan), at t = 160 Ma and t = 100 Ma:

$$u_r(160\,\text{Ma}, 14^\circ\text{N}, 30^\circ) = 635\,\text{m}; \qquad u_r(100\,\text{Ma}, 14^\circ\text{N}, 30^\circ) = 1156\,\text{m}$$

leading to a vertical uplift of about $\frac{du_r}{dt} \simeq 8.7\,\text{m/Myr}$. This uplift is due to the increase of plate velocities around the Pacific, that is to say to the increase of the quantity of masses subducted along the ring of subduction.

Such an uplift has also been predicted in the dynamic topography histories of the Kaapvaal craton derived by *Zhang et al*. [2012] and by *Flament et al*. [2014], as well as observed in the thermal histories inferred by *Flowers and Schoene* [2010] and converted to burial depths. We plot on Figure 9f the temporal evolution of the uplift at the previous point (black star located in Sudan) and at a point of coordinates $(-25^\circ\text{S}, 22^\circ\text{E})$ (black filled square located in the Kaapvaal craton). We obtain a dynamic uplift variation of ∼500 m between 160 and 100 Ma, which then decreases in Sudan, while it remains constant in the Kaapvaal craton [see also *Flament et al*., 2014, Figure 8e, orange curve].

Similar to the region of Sudan, we predict that Northern Africa (black circle in Figures 9d and 9e) is dynamically uplifted from ∼ 160 Ma to ∼100 Ma (with a rate ∼9 m/Myr) and then undergoes subsidence (dynamic topography becoming less positive) with a rate ∼−5 m/Myr (dotted line in Figure 9f). This subsidence seems to be consistent with the observed flooding of Northern Africa between 100 and 50 Ma [*Guiraud et al*., 2005], over a period during which sea level, after reaching a maximum during the Cenomanian, decreased [*Haq et al*., 1987; *Haq and Al-Qahtani*, 2005], while remaining in a context of very high level compared to the Early Triassic for example. Note that the period 100–50 Ma is typically a postrift period and consequently a thermal subsidence may be expected in addition to our predicted dynamic topography.

Looking more precisely at the dynamic topography over the western part of the African plate and over the South American plate 160 Ma ago (Figure 9d), we find topographic isocontours ranging from −800 m up to 400 m aligned with the subduction zone along the west coast of the South American plate (see also example 2.3.3). These results are similar with those obtained by *Flament et al*. [2014] (see their Figure 6 at 130 Ma) and suggest that the subduction zone being almost perpendicular to the future opening of the South Atlantic Ocean, it cannot be at the origin of such a rift.

The present-day topography is very similar to the one obtained by *Lithgow-Bertelloni and Silver* [1998] with their slab model (their Figure 1b) but does not reproduce the anomalous elevation of the southern and eastern African plateaus [*Moucha and Forte*, 2011]. Our dome model likely underestimates the upwelling mantle flow that dynamically supports the anomalously high elevation of the African superswell.

3.2. Lithospheric Stresses

The maximal lithospheric shear stress and the associated normal stress are plotted respectively on Figures 10 and 11 since 280 Ma. Their magnitudes are about a few tens of MPa, result similar to the ones of *Ghosh et al*. [2013] who predicted deviatoric stresses ranging between 20 and 70 MPa. The largest stresses occurred above the peri-Pacific girdle of subduction and the regions of the domes. The maximal shear stress above the Tethyan subduction (about 40 MPa) occurred during the Middle Triassic when the convergence rate at the active margin was high (about 10 cm/yr). Since the Jurassic Period, the convergence rate has been less than 4 cm/yr, leading to maximal shear stress less than 20 MPa, i.e., much smaller than the ones above the peri-Pacific ring of subduction (∼80 MPa).

From 280 Ma up to 160 Ma, we find in Africa a theoretical NW-SE faults orientation trend remaining constant through time. This direction is related to the direction of the subduction zone along the West coast of South America, which is the most active part of the ring of subduction during this period. Between 150 and 90 Ma, subduction becomes more active along the southern margin of Gondwana involving a change in the direction of the faults toward an E-W direction, i.e., toward a direction parallel to this subduction zone.

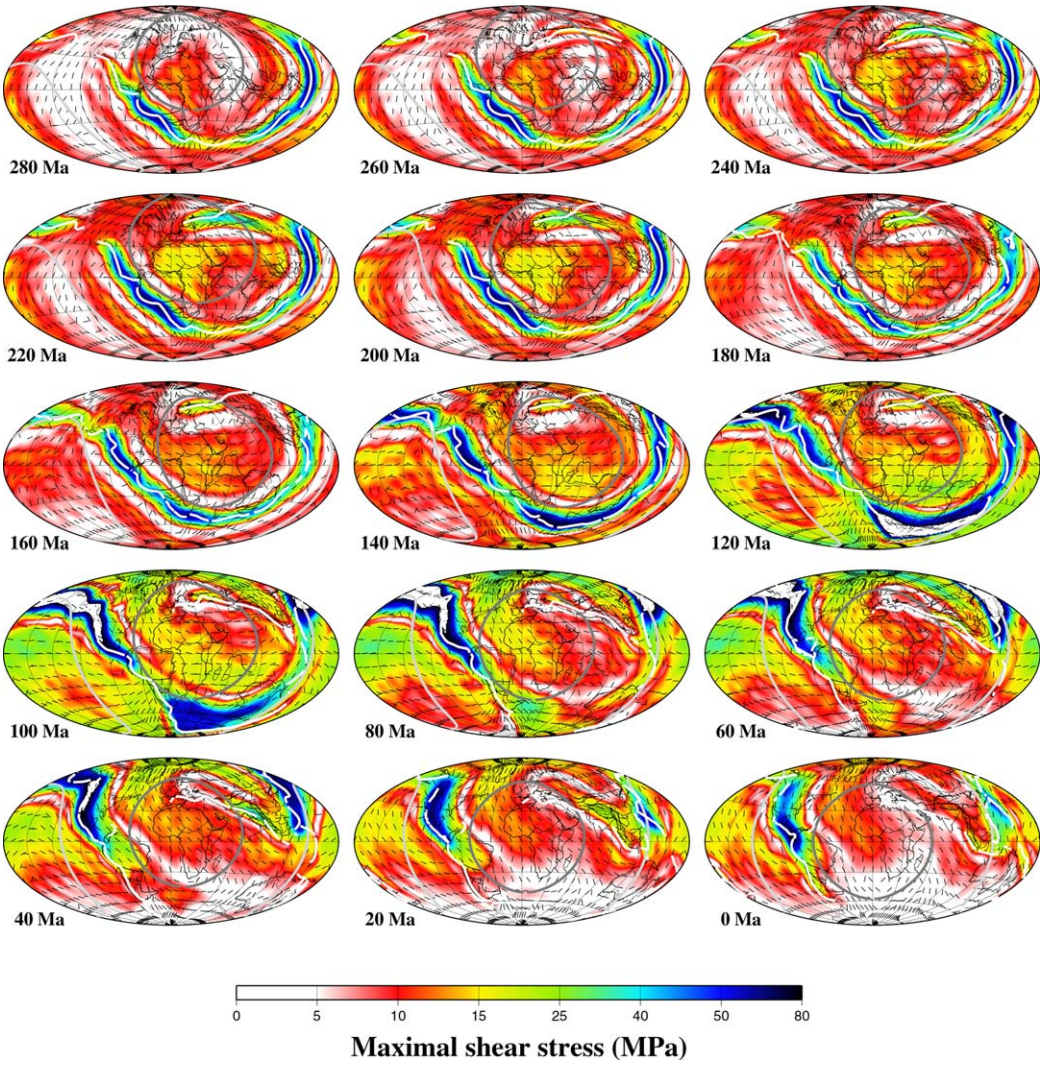

Figure 10. Maximal shear stress (in MPa) at different periods of time, in the fixed African plate reference frame. The black solid lines denote the fault plane. The grey small circles feature the position of the domes at the bottom of the mantle and the white lines the subduction zones (Hammer projection).

After 80 Ma, the dominant subduction zone is along the West coast of North America (in a NW-SE direction), and the azimuth of the faults plane becomes again NW-SE.

Let us now discuss in more details the shear stresses over and around Africa.

In Figure 12, we show a zoom of the lithospheric shear stress map, over Africa, 190, 120, 100, and 80 Ma ago. The normal stresses are extensive over this region and the amplitude of the maximal shear stresses is about 20 MPa.

1. 190 Ma ago, in the north-western part of Africa, the NW-SE direction of our computed fault plane is almost perpendicular to the observed rift direction between Africa and North America (Figure 12a): the driving force associated with the mantle density heterogeneities due to subducted slabs and domes is not the most likely candidate to explain the opening of the Central Atlantic Ocean, 200 Ma ago. It is worth noting that the Late Triassic Central Atlantic rift system was exactly superimposed to the Alleghenian-Variscan orogen. This weak zone was the site of strong body forces linked to orogenic collapse and slab detachment below the Alleghenian suture.
2. By contrast, the quasi East-West direction at 120 Ma of our theoretical fault planes in the eastern part of Africa is in good agreement with the observed direction of spreading between Madagascar and Africa, within the Mozambique channel [*Ségoufin and Patriat*, 1980]. The isochrons and transform fault systems

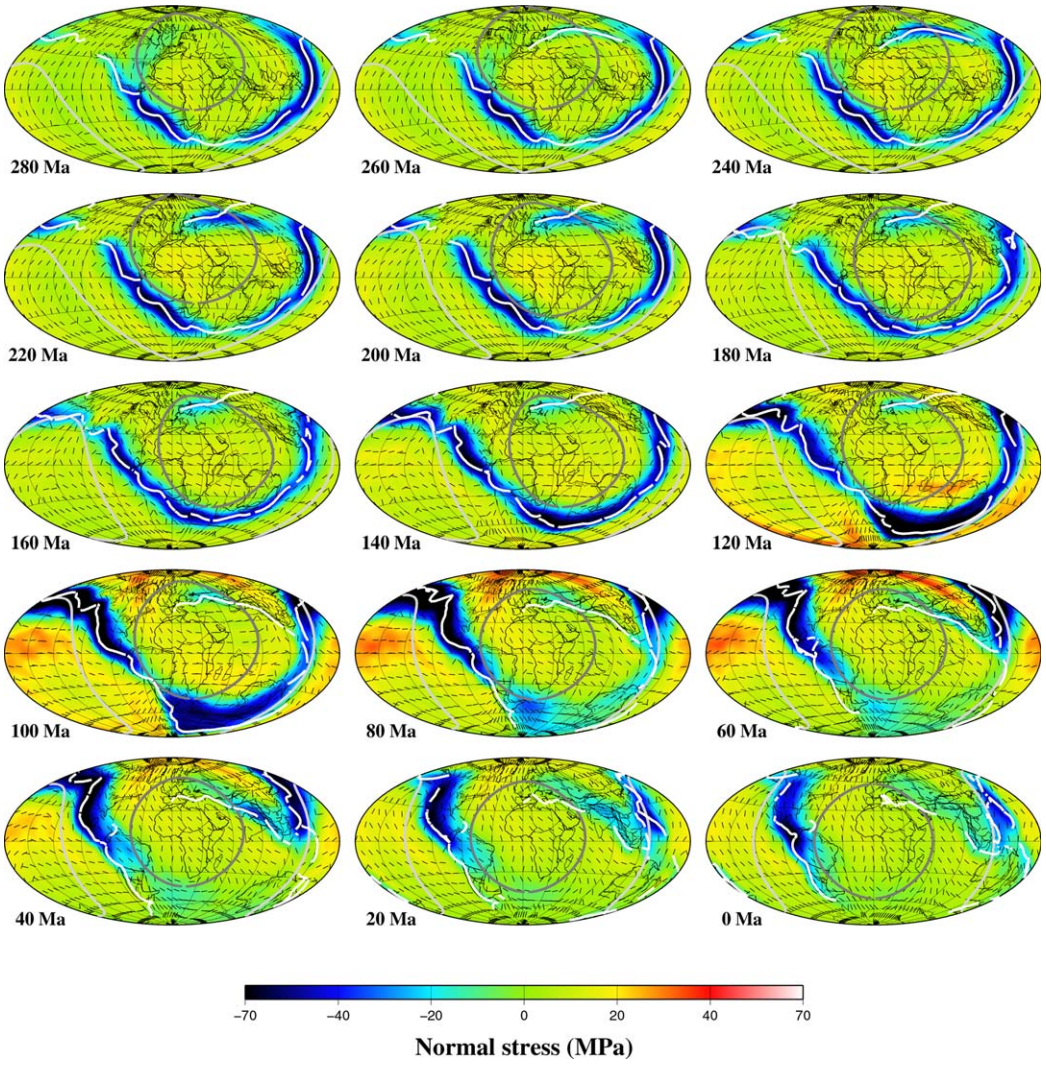

Figure 11. Normal stress (in MPa) at different periods of time, in the fixed African plate reference frame. The black solid lines denote the fault plane. The grey small circles feature the position of the domes at the bottom of the mantle and the white lines the subduction zones (Hammer projection).

are plotted as cyan lines in Figure 12b. We have represented as small green arrows the motion on some transform faults, while the general opening direction is represented by a large green arrow. This extension may be related to the opening of the Indian Ocean, which started 180 Ma ago, when Madagascar, Australia, India, and Antarctica split from the African coast [*Reeves*, 2014]. Note also that, in West Africa, the stress field is extremely well aligned with the later forming Equatorial Fracture Zone between Africa and Central America.

3. From 120 Ma, Australia and Antartica started to separate from Madagascar-India (large green arrow in Figure 12c). The rifting between Australia and Madagascar/India seems to be caused by the stress field imposed by our proposed subduction-doming system: the East-West azimuth of the computed fault planes, 100 Ma ago, is correlated with the direction of the isochrons (cyan line) and the extension represented as small green arrows in Figure 12c) between, on one side India and on the other side Antartica and Australia [*Gibbons et al*., 2013].
4. 84 Ma ago, India started to separate from Madagascar and moved northward, in a direction almost perpendicular to our fault plane (green arrow in Figure 12d).

We obtain, in our model, a permanent extensional regime during the Mesozoic and the Cenozoic over the African continent. The quantity of masses subducted along the girdle of subduction is a crucial parameter

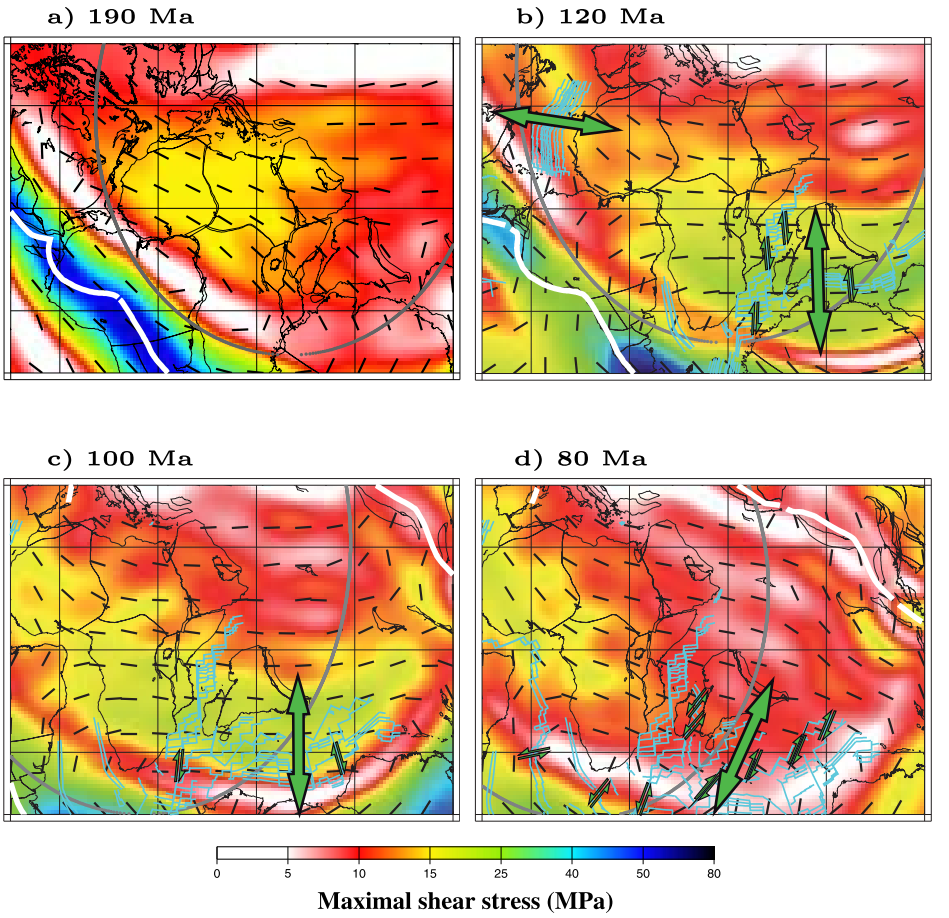

Figure 12. Extensive stress over Africa, in the fixed African plate reference frame (Mercator projection), (a) 190Ma, (b) 120Ma, (c) 100Ma, and (d) 80Ma ago. The black solid lines denote the fault plane, the cyan lines are isochrons (from Gplates) [*Seton et al*., 2012]. The green arrow represents the opening between two blocks. The grey small circle features the position of the African dome at the bottom of the mantle and the white thick lines the subduction zones.

to determine the direction of the faults in the region comprised within the ring. The presence of a dome at the bottom of the mantle beneath this region does not perturb this direction but reinforces the amplitude of the extensive stress allowing some possible breaks.

In Figure 13, we superimpose the maximum predicted shear stress field (black solid isoline with contour intervals of 5 MPa) and fault planes (maroon line), 125 Ma ago, to a reconstructed geological map with the major rifts of the African continent [from *Guiraud et al*., 2005; *Frizon de Lamotte et al*., 2015]: the Early Cretaceous Rift system is plotted in green. The direction of faults plane 125 Ma ago may be correlated, to first-order, with the observed direction of the NW/NE African rifts during the Mesozoic, which are, from west to east: the equatorial segment of the Central Atlantic, Benue, Doba, Birao, Muglad, and Anza rifts [*Guiraud and Maurin*, 1992]. However, we do not find a correlation for the opening rifts of the North Atlantic and the South Atlantic, where other mechanisms have to be proposed. For example, the significant gap observed in the austral segment of the South Atlantic may be explained by a local disturbance by the Etendeka-Parana Large Igneous Province (LIP) (see below).

Note that there is no ridge push or forces related to collision in our approach and that the sources are only the mantle density heterogeneities associated with both subducted plates and large-scale domes at the bottom of the mantle. Our model assumes a viscous lithosphere: this hypothesis, based on geoid observations, is valid only for large length-scale mantle dynamic and the rheology of the lithosphere should be more complex for investigating local deformations. But in any case, for such a soft lithosphere, we find that mantle mass anomalies can involve stresses at the surface, reaching value as large as 20 MPa, i.e., surpassing the failure limit of rocks in tension (about 4 MPa) [*Chinnery*, 1964].

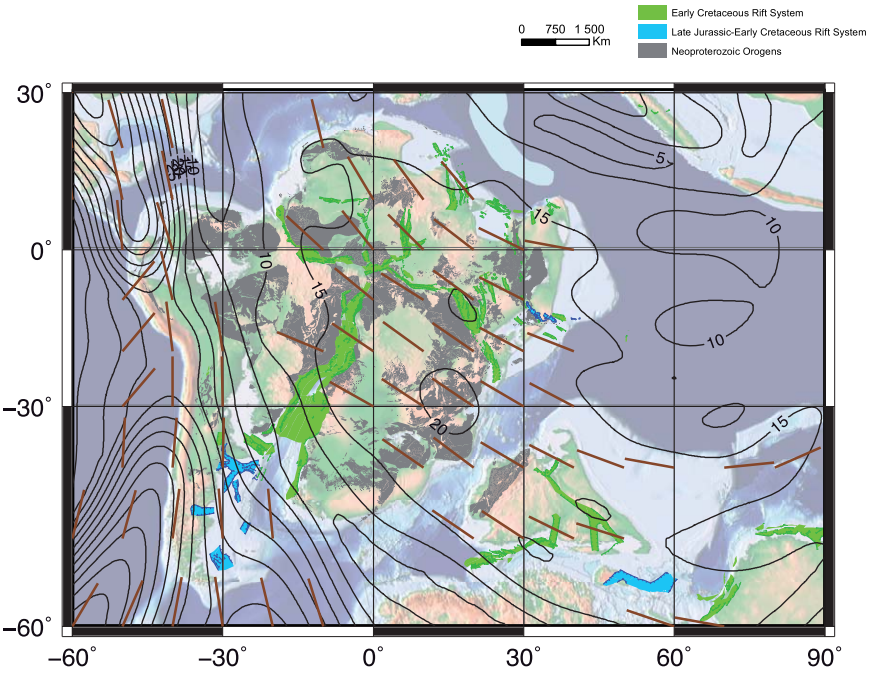

Figure 13. Maximal shear stress contour line (black solid line with contour intervals of 5 MPa) and fault planes (maroon line), 120 Ma ago (Mercator projection). The figure is in a paleomagnetic reference frame [*Schettino and Scotese*, 2005]. The background of the map is from Plate tectonic maps and Continental drift animations by C. R. Scotese, PALEOMAP Project (www.scotese.com). We used the software ArcGis.

Consequently, we confirm that in addition to the two mechanisms usually invoked to be the cause of the extensional regime and the thinning of the lithosphere (tectonic forces acting at plate boundaries [*McKenzie*, 1978] and thermal erosion of the lithosphere [*Burke and Dewey*, 1973]), the mantle buoyancy forces associated with past subduction have to be taken into account.

To discuss the relative influence of local disturbances (for example the Tristan hotspot and the associated Parana-Etendeka LIP 130Ma ago, the Kerguelen hotspot with the Rajmahal traps 120 Ma ago, the Marion hotspot and the late Cretaceous magmatism in Madagascar 90–80 Ma ago, blue spots on Figure 14a), we superimpose to our slabs + domes model the effect of a plume at the top of the upper mantle.

We simply model the plume as a spherical head with a radius of about 250 km and a trailing conduit whose volume is negligible. The density contrast is set to $-30\,\mathrm{kg/m^3}$. The center of the spherical head is such that the top of the plume head is just at the base of the lithosphere (cf., subsection 2.3.2).

1. We first superimpose a plume located at −20°S, 12°E (the position of the Tristan hotspot, 140 Ma ago) to our mantle mass anomalies 140 Ma: we find an extension above the plume, with a maximal uplift of about 800 m, and a maximal extensive stress of about 70 MPa (Figure 14b). The direction of the fault planes is aligned with the direction of the future opening of the South Atlantic Ocean, i.e., with the direction of separation between two plates as shown from the tectonic flowline [see *Müller et al*., 2016, Figure 8c].
2. We also superimpose a plume located at −17.2°S, 68.9°E (the position of the Kerguelen hotspot 130 Ma ago) [*Curray and Munasinghe*, 1991; *Balmer et al*., 2015] to our mantle mass anomalies: we find an extension above the plume, with a maximal uplift of about 1100 m and a maximal extensive stress of about 70 MPa (Figure 14c). This plume was located at the triple junction between Greater India, Australia, and Antarctica before the breakup of eastern Gondwana and consequently this effect may have played an important role in the separation of Australia-Antartica from Madagascar-India.
3. We then superimpose a plume located at −24°S, 46°E (the position of the Marion hotspot 90 Ma ago, beneath southeast Madagascar) [*Storey et al*., 1995; *Torsvik et al*., 1998] to our mantle mass anomalies 90 Ma ago: we find an extension above the plume and a maximal extensive stress of about 70 MPa (Figure 14d). Consequently, this effect has to be taken into account to understand the mechanism at the origin

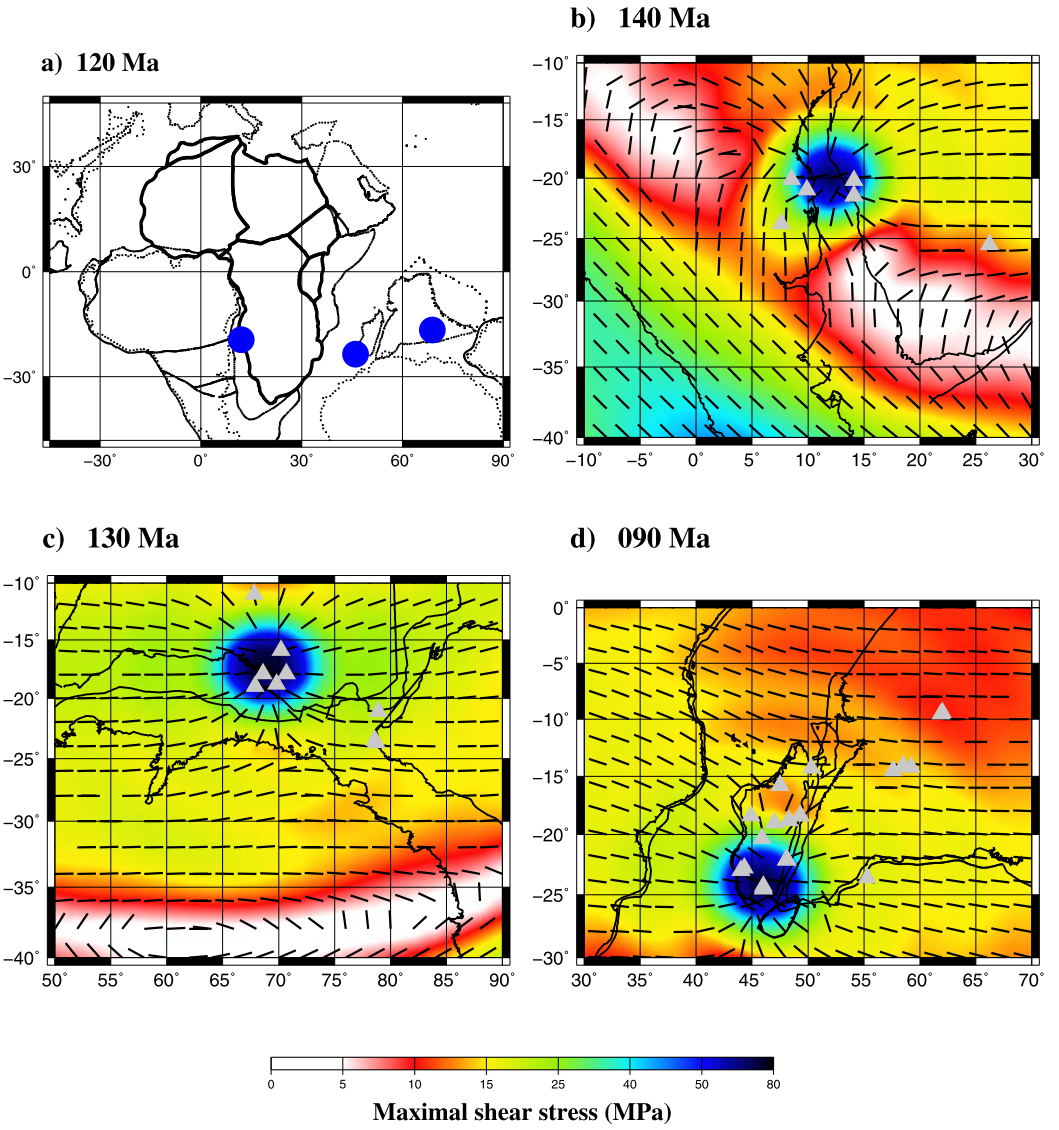

Figure 14. (a) Positions of the Tristan hotspot 140Ma ago, the Kerguelen hotspot 130 Ma ago and the Marion hotspot 90 ago (blue spots), superimposed to the paleogeography 120 Ma ago in a reference frame linked to the fixed African plate. Maximal shear stress induced by our slabs + domes geodynamic model and a local plume (Mercator projection): (b) 140 Ma ago, influence of the Tristan plume before the appearance of Parana-Etendeka LIP and the opening of the South Atlantic Ocean: the grey triangles represent the volcanism data from 150 to 140 Ma. (c) 130 Ma ago: influence of the Kerguelen plume before the appearance of Rajmahal traps and the separation of Australia-Antartica from Madagascar-India: the grey triangles represent the volcanism data from 130 to 120 Ma. (d) 90 Ma ago: influence of the Marion plume before the appearance of magmatism in Madagascar and the separation of India from Madagascar: the grey triangles represent the volcanism data from 90 to 80 Ma.

of the separation of India with respect to Madagascar and the initiation of its northward fast movement [*Cande and Stegman*, 2011].

4. Finally, we did not perform such modeling below the future zone of opening of the Central Atlantic Magmatic Province (CAMP), 200 Ma ago. Indeed, we have reconstructed the position of the primary hotspots in the geological past in our fixed African plate reference frame, and found that the three hotspots that could have been in the CAMP region 210 ago (Fernando, Cape Verde or Canary) were too far (from 1500 to 5000 km) from the traces of the intraplate volcanism of the CAMP. Consequently, even if large volumes of LIP are associated with Central Atlantic breakup [e.g., *Davaille et al.*, 2005], it seems difficult to relate them to any track showing the existence of a plume. CAMP may be associated with warming under a supercontinent [*Coltice et al.*, 2007] in a weak zone linked to the Alleghenian suture.

The extension directions predicted by our model are only induced by the buoyancy forces related to mass anomalies within the mantle and appear at the surface before the first traces of volcanism and the emptying of the plume head at the origin of the flood basalts. It is difficult to estimate the characteristic time of the delay between the first significant stresses and the massive volcanism because it strongly depends on the amplitude of the thermal anomaly, its size, and the viscosity of the upper mantle. The order of magnitude of the stresses is similar to the one obtained for the mantle density heterogeneities due to subducted lithosphere and to long-wavelength upwellings. This leads us to think that there is a causal relation between hotspot activity and rifting [*Frizon de Lamotte et al*., 2015]): the hotspot heating could have weakened the lithosphere all along its trajectory.

4. Conclusions

We have used a simple geodynamic model in which the time-dependent mantle density heterogeneities are modeled using plate reconstructions and geological constraints. We assume that subducted slabs sink vertically into the mantle down to the CMB, with a velocity reduction below the transition zone and a thickening with a 4 factor within the lower mantle. Two large-scale domes at the bottom of the lower mantle are also taken into account and are modeled using the surface occurrence of intraplate volcanism. We computed the associated dynamic topography and find that slabs create broad topographic depressions (about -2000 m) which may explain the appearance of some basins since the Permian, related to the drift of a continent over a slab. Domes situated at the bottom of the mantle create a large-wavelength positive topography ($\simeq 200$ m) as observed nowadays above of Africa and Polynesia. We find that the peri-Pacific girdle of subduction creates a large-wavelength positive topography (about 600m) at the center of the ring they form situated roughly over Africa.

The associated lithospheric stresses show that the normal stresses above the domes are extensive, with radial fracture directions. For a girdle of subductions, the normal stresses are compressive above the subductions zones and extensive within the small circle they are delimiting. The fractures situated just above the subduction zone are aligned with the azimuth of the slab. They are concentric in the middle of the small circle. The superimposition of the extension in the middle of the peri-Pacific ring of subductions with the one induced by the African dome leads consequently to a permanent extensional regime over Africa and Indian Ocean. This extension creates faults with azimuth directions depending on the direction of the most active part of the ring of subductions. We obtain fractures with NW-SE azimuth during the period 275–165 Ma, parallel to the direction of the subduction zone along the West coast of South America which is very active during this period. Between 155 and 95 Ma, the subductions become more active along the Australian coast involving a change in the direction of the faults toward an E-W direction, i.e., parallel to this subduction zone, in agreement with the observed fault systems between Africa and India, Antartica and Australia.

We correlate our shear stress over Africa and Indian Ocean with the observed Mesozoic direction of the rifts. The role of three primary hotspots is finally evidenced, which superimpose or relocalize extension to facilitate the opening of ocean basins.

Further improvements of this work will introduce regional mantle density heterogeneities, with smaller wavelengths than the ones investigated in this paper. A more complex rheology of the lithosphere will also be taken into account. Most studies of mantle dynamics, including ours, are based on geoid observations at the global scale and assume very soft lithospheres. In this paper, we have set a viscosity about 1.1×10^{22} Pa.s which can be considered as an equivalent viscosity that permits us to fit geoid anomalies with good accuracy at a global scale, without considering probable viscosity lateral variations in the lithosphere or tectonic plate motions [*Richards and Hager*, 1984; *Ricard et al*., 1993]. To work at a regional scale, such a low viscosity may not be appropriate. As a first test, we have introduced an elastic thin crust at the top of the lithosphere and computed the deformations induced by a spherical plume in the upper part of the mantle. It changes the amplitude of the surface deformations, but not its geometry. However, further work is required to better take into account the presence of weak zones, even if the simplicity of our model of mantle dynamics prevents us from reaching this level of resolution.

Appendix A: Maximal Shear Stress and Normal Stress

To compute the maximal shear stress and the dip p and azimuth A of the associated fault plane, we work in the reference frame of the Principal Stresses Axis. The eigenvalues $(\tilde{\sigma_1}, \tilde{\sigma_2}, \tilde{\sigma_3})$ and the eigenvectors $(\vec{V}_1, \vec{V}_2, \vec{V}_3)$ associated with our viscous stress tensor are:

$$\tilde{\sigma_1} = \frac{\sigma^f_{\varphi\varphi} + \sigma^f_{\theta\theta}}{2} + \frac{1}{2}\Delta \quad \text{with} \quad \vec{V}_1 = \frac{1}{\sqrt{1 + \left[\frac{(\sigma^f_{\varphi\varphi} - \sigma^f_{\theta\theta}) - \Delta}{2\sigma^f_{\theta\varphi}}\right]^2}} \begin{pmatrix} 0 \\ -\frac{(\sigma^f_{\varphi\varphi} - \sigma^f_{\theta\theta}) - \Delta}{2\sigma^f_{\theta\varphi}} \\ 1 \end{pmatrix}$$

$$\tilde{\sigma_2} = \frac{\sigma^f_{\varphi\varphi} + \sigma^f_{\theta\theta}}{2} - \frac{1}{2}\Delta \quad \text{with} \quad \vec{V}_2 = \frac{1}{\sqrt{1 + \left[\frac{(\sigma^f_{\varphi\varphi} - \sigma^f_{\theta\theta}) + \Delta}{2\sigma^f_{\theta\varphi}}\right]^2}} \begin{pmatrix} 0 \\ -\frac{(\sigma^f_{\varphi\varphi} - \sigma^f_{\theta\theta}) + \Delta}{2\sigma^f_{\theta\varphi}} \\ 1 \end{pmatrix}$$

$$\tilde{\sigma_3} = 0 \quad \text{with} \quad \vec{V}_3 = \begin{pmatrix} 1 \\ 0 \\ 0 \end{pmatrix}$$

where we note

$$\Delta = \sqrt{(\sigma^f_{\varphi\varphi} - \sigma^f_{\theta\theta})^2 + 4(\sigma^f_{\theta\varphi})^2} > 0$$

In this reference frame of the Principal Stresses Axis, we use the Mohr's Circle, a tool to visualize relationships between normal and shear stresses, and to estimate the maximal stresses.

A1. Mohr's Circle

We note σ_1, σ_2, and σ_3 are the principal stresses such as:

$$\sigma_1 > \sigma_2 > \sigma_3$$

and n_1, n_2, and n_3 are the components of the normal to the fault plane in the principal stresses axes. The normal stress σ and the shear stress τ may be written:

$$\sigma = \sigma_1 n_1^2 + \sigma_2 n_2^2 + \sigma_3 n_3^2$$
$$\tau^2 + \sigma^2 = \sigma_1^2 n_1^2 + \sigma_2^2 n_2^2 + \sigma_3^2 n_3^2$$

Consequently the components of the normal to the fault plane may be written:

$$n_1^2 = \frac{(\sigma_3 - \sigma)(\sigma_2 - \sigma) + \tau^2}{(\sigma_1 - \sigma_3)(\sigma_1 - \sigma_2)}$$
$$n_2^2 = \frac{(\sigma_1 - \sigma)(\sigma_3 - \sigma) + \tau^2}{(\sigma_2 - \sigma_1)(\sigma_2 - \sigma_3)}$$
$$n_3^2 = \frac{(\sigma_2 - \sigma)(\sigma_1 - \sigma) + \tau^2}{(\sigma_3 - \sigma_1)(\sigma_3 - \sigma_2)}$$

If we plot τ as a function of σ for different values of n_1, n_2, and n_3, we obtain the classical Mohr's Circle.

The maximal shear τ_{max} is reached for $\sigma = \frac{\sigma_1 + \sigma_3}{2}$ and is equal to $\tau_{\max} = \frac{\sigma_1 - \sigma_3}{2}$. For these values, the components of the normal in the eigenvectors basis are:

$$n_1 = \frac{1}{\sqrt{2}}, \quad n_2 = 0 \quad n_3 = \frac{1}{\sqrt{2}}$$

A2. Maximal Shear and Associated Normal in the Spherical Basis

To use these results in our study, we have to order our stresses.

Three cases are possible:

- $\tilde{\sigma_1} > \tilde{\sigma_2} > 0$

In this case $\tau_{max} = \frac{\tilde{\sigma_1}}{2}$ and the normal is:

$$\vec{n} = \frac{1}{\sqrt{2}}(\vec{V}_1 + \vec{V}_3)$$

and the dip and the azimuth are:

$$p = 45^o; \quad \text{and} \quad A = \arctan\left[-\frac{(\sigma^f_{\varphi\varphi} - \sigma^f_{\theta\theta}) - \Delta}{2\sigma^f_{\theta\varphi}}\right]$$

- $\tilde{\sigma_1} > 0 > \tilde{\sigma_2}$

In this case $\tau_{max} = \frac{\tilde{\sigma_1} - \tilde{\sigma_2}}{2}$ and the normal is:

$$\vec{n} = \frac{1}{\sqrt{2}}(\vec{V}_1 + \vec{V}_2)$$

and the dip and the azimuth are: $p = 90^o$ and

$$\tan A = \frac{1}{\sqrt{2}} \frac{\frac{-\sigma^f_{\varphi\varphi} + \sigma^f_{\theta\theta} + \Delta}{\sqrt{4(\sigma^f_{\theta\varphi})^2 + [\sigma^f_{\varphi\varphi} - \sigma^f_{\theta\theta} - \Delta]^2}} + \frac{-\sigma^f_{\varphi\varphi} + \sigma^f_{\theta\theta} - \Delta}{\sqrt{4(\sigma^f_{\theta\varphi})^2 + [\sigma^f_{\varphi\varphi} - \sigma^f_{\theta\theta} + \Delta]^2}}}{\frac{1}{\sqrt{1 + [\frac{(\sigma^f_{\varphi\varphi} - \sigma^f_{\theta\theta}) - \Delta}{2\sigma^f_{\theta\varphi}}]^2}} + \frac{1}{\sqrt{1 + [\frac{(\sigma^f_{\varphi\varphi} - \sigma^f_{\theta\theta}) + \Delta}{2\sigma^f_{\theta\varphi}}]^2}}}$$

- $0 > \tilde{\sigma_1} > \tilde{\sigma_2}$

In this case $\tau_{max} = -\frac{\tilde{\sigma_2}}{2}$ and the normal is:

$$\vec{n} = \frac{1}{\sqrt{2}}(\vec{V}_2 + \vec{V}_3)$$

and the dip and the azimuth are:

$$p = 45^o \quad \text{and} \quad A = \arctan\left[-\frac{(\sigma^f_{\varphi\varphi} - \sigma^f_{\theta\theta}) + \Delta}{2\sigma^f_{\theta\varphi}}\right]$$

Appendix B: Geodynamic Model

We start from our simple geodynamic model [*Greff-Lefftz and Besse*, 2012], in which we combined contributions due to subducted lithosphere and long-wavelength upwellings.

B1. Downwelling

We use plates-motion reconstructions since 400 Ma and under the assumption that subducted slabs sink vertically into the mantle [*Ricard et al*., 1993], we derive a model of time-dependent mantle density heterogeneities. Note that this assumption does not exclude any apparent horizontal slab motion in the mantle which may exist because of the trench migration: there is possible inclination of deep slab structure in region with migration of the active continental margin, while the slabs are more or less vertical in regions with stable subduction zones [see *Lithgow-Bertelloni and Richards*, 1998, Figure 5].

Following [*Ricard et al*., 1993], we assume a linear relationship between the plate velocity and the thickness of the subducted lithosphere: a 10 cm/yr slab is 100 km thick and a 0 cm/yr slab is 33 km thick. A threshold of 2 cm/yr is used for the slab velocity. We set the density contrast between the cold slab and the ambient mantle to 80 kg/m^3, and neglecting thermal diffusion and shear heating, we suppose that this excess density remains constant while a slab is sinking. The diving velocity of the slabs is equal to the surface convergence velocity of the plates v_s when the sinking slabs are in the upper mantle, whereas it is equal to $\frac{v_s}{V_R}$

Table B1. Euler Poles and Angles Used for the Different Subductions of our Model at the Different Stages. P1 and P2 Are the West Pacific Subduction Zone and Sp the Peri-Pacific Zone. Ht1 is the Paleo-tethyan Convergence Zone, T2 the Neo-Tethyan Convergence Zone and T1 and T1b the New Convergence Zone Appearing after 230 Ma

Subduction	Latitude	Longitude	Euler Angle/Myr	t_{min}	t_{max}
HT_1	−36	−110	0.7°/Myr	410 Ma	380 Ma
HT_1	3	−166	2.3°/Myr	380 Ma	360 Ma
HT_1	80	115	0.6°/Myr	360 Ma	320 Ma
HT_1	30	−150	0.1°/Myr	320 Ma	310 Ma
P_1	76	223	1°/Myr	410 Ma	340 Ma
P_1	76	223	0.8°/Myr	340 Ma	300 Ma
SP	56	260	0.8°/Myr	300 Ma	200 Ma
T_2	23	354	1°/Myr	270 Ma	230 Ma
T_1	23	354	0.4°/Myr	230 Ma	120 Ma
T_{1b}	70	60	0.3°/Myr	230 Ma	120 Ma

when the slabs are in the lower mantle. In order to conserve thermal buoyancy, we assume that slabs are folded or thickened in proportion to this velocity factor V_R. We set the viscosity ratio between lower and upper mantle to 40 involving a factor V_R around 4 (Figure 4a). To be self-consistent, our model of mantle density heterogeneities must include all the slabs over a period larger than the characteristic time needed for a slab to sink through the depth of the mantle: *Ricard et al*. [1993] and more recently *van der Meer et al*. [2010] suggest that an appropriate mantle transit time is of order 100–200 Myr. Such a slab heterogeneity model is correlated with current tomographic models at large wavelength [*Ricard et al*., 1993, 2005]. We thus investigated plate motions during the last 410 million years from geological, paleomagnetic, and subduction related calc-alkaline volcanism data, to model the temporal evolution of mantle density heterogeneities associated with subductions since 280 Ma.

For the period between 410Ma and 200Ma, we keep our previous plates motions [*Greff-Lefftz and Besse*, 2012]. In our previous paper, we used 14 interpolated plate stages between 410 and 130 Ma. Here, we build our mantle density heterogeneities models using stages each lasting 10 Myr. The Euler poles and the time-derivative of the angles used for the different subductions are given in Table B1: P_1 is the West Pacific subduction zone and SP the peri-Pacific zone. HT_1 is the Paleo-Tethyan convergence zone, T_2 is the Neo-Tethyan convergence zone and T_1, and T_{1b} is the new convergence zone appearing after 230 Ma (T_1 and T_{1b} are, respectively, the West part (longitude less than 90°) and the East part (longitude greater than 90°) of the subduction zone).

For the period between 200 Ma and the present, we start from a compilation of plates motions by *Seton et al*. [2012]: we first extract the position of the subduction zones and the plates velocities from GPlates software and then we compute slabs velocities in the upper mantle from the local convergence rate (i.e., we compute the components of the velocity along the perpendicular to the segment of the subduction zone). Nevertheless, for the period 200–120 Ma, we modify the position of the Neo-Tethys subduction proposed by *Seton et al*. [2012], in order to take into account the Mongol-Okhotsk ocean situated between the Amuria North China block and Silesia [*Cogné et al*., 2005]: we keep the position of the subduction zone along the Siberia margin with Euler poles and angle of T_1 and T_{1b} until 120 Ma. For each stage, we have plotted in Figure B1 the position of the subductions zones as well as the subduction related calc-alkaline volcanism (black triangle).

We have compared our model with other recent models of plate tectonics in the late Paleozoic integrated Gplates [*Domeier and Torsvik*, 2014; *Matthews et al*., 2016], for each stages lasting 10 Myr. The only notable difference is the presence, in their models, of a subduction zone along the west part of the North America plate between 410 and 300Ma. Nevertheless, the relative velocity, between the Panthalassa plate and the North America plate, perpendicular to this subduction zone was very small and consequently, only little mass subducted into the mantle at this place. This is consistent with the fact that only a few volcanic activity (if any) can be found in this region during this period, suggesting that, following our assumption, there was no or only little subduction on this margin. This is also in good agreement with the collisional context prior to the Hercynian collision, when Laurussian and Gondwanan continents collided.

We plot in Figure B2 the average velocity of the slabs starting to sink in the upper mantle as a function of time. It is ranging from 3 to 10 cm/yr, with the larger values in the Early Cretaceous Period and with a mean value during the past 400 Ma about 5.7 cm/yr. The average sinking rates obtained for the lower mantle is a

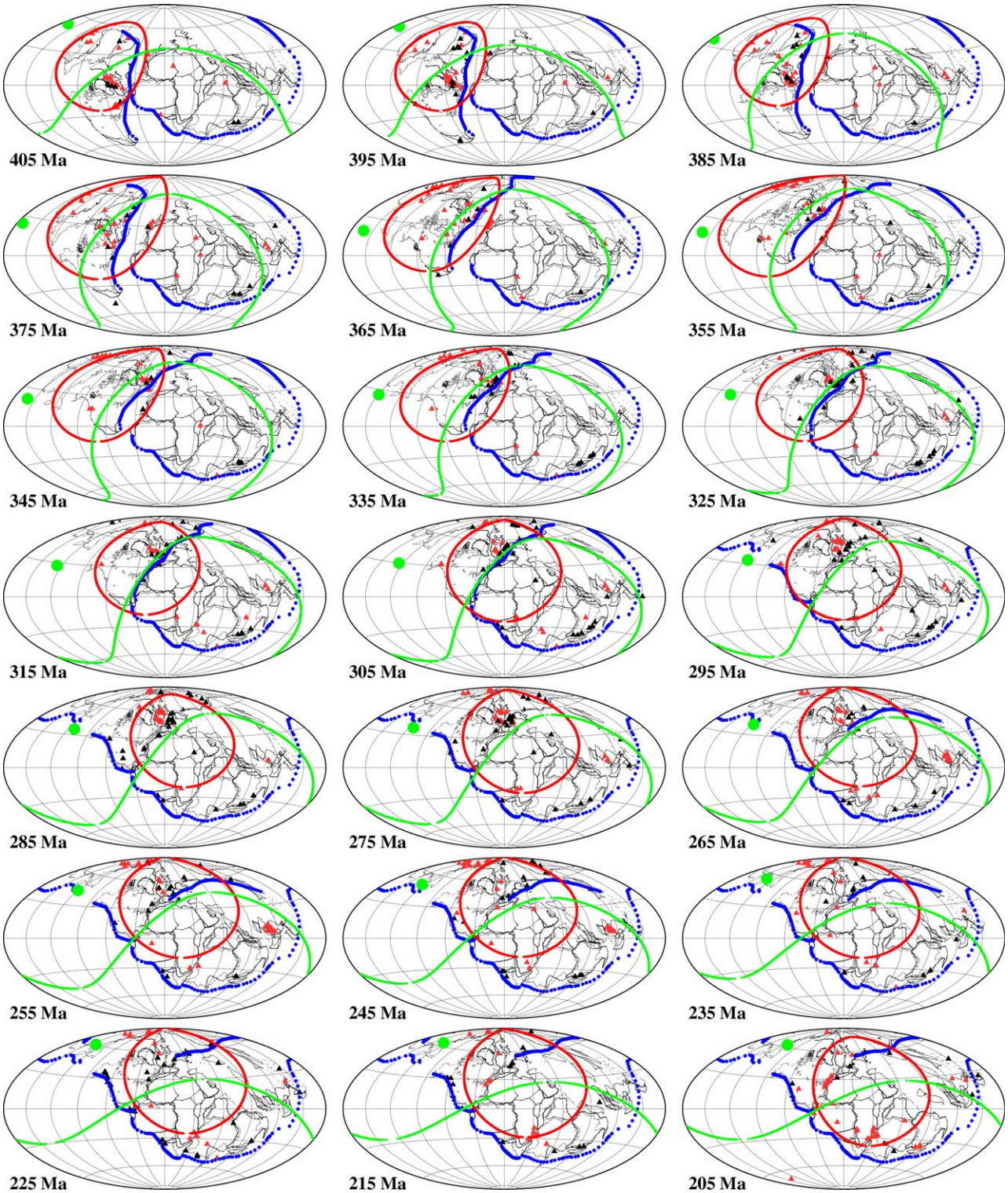

Figure B1. Paleoreconstructions since 410 Ma (with respect to African plate kept fixed); red triangles: intraplate volcanism; black triangles: subduction volcanism; the red circle represents our modeled area of intraplate volcanism above the African dome; blue lines: subduction zones; the green great circle and its pole (green dot) are the paleomagnetic equator and the paleomagnetic pole (Hammer projection).

quarter of this value and is consequently of about 1.4 cm/yr, that-is-to-say with the same order of magnitude than recent attempts at constraining rates from tomography, giving roughly between 1 and 1.5 cm/yr [*van der Meer et al.*, 2010; *Steinberger et al.*, 2012; *Butterworth et al.*, 2014; *Domeier et al.*, 2016].

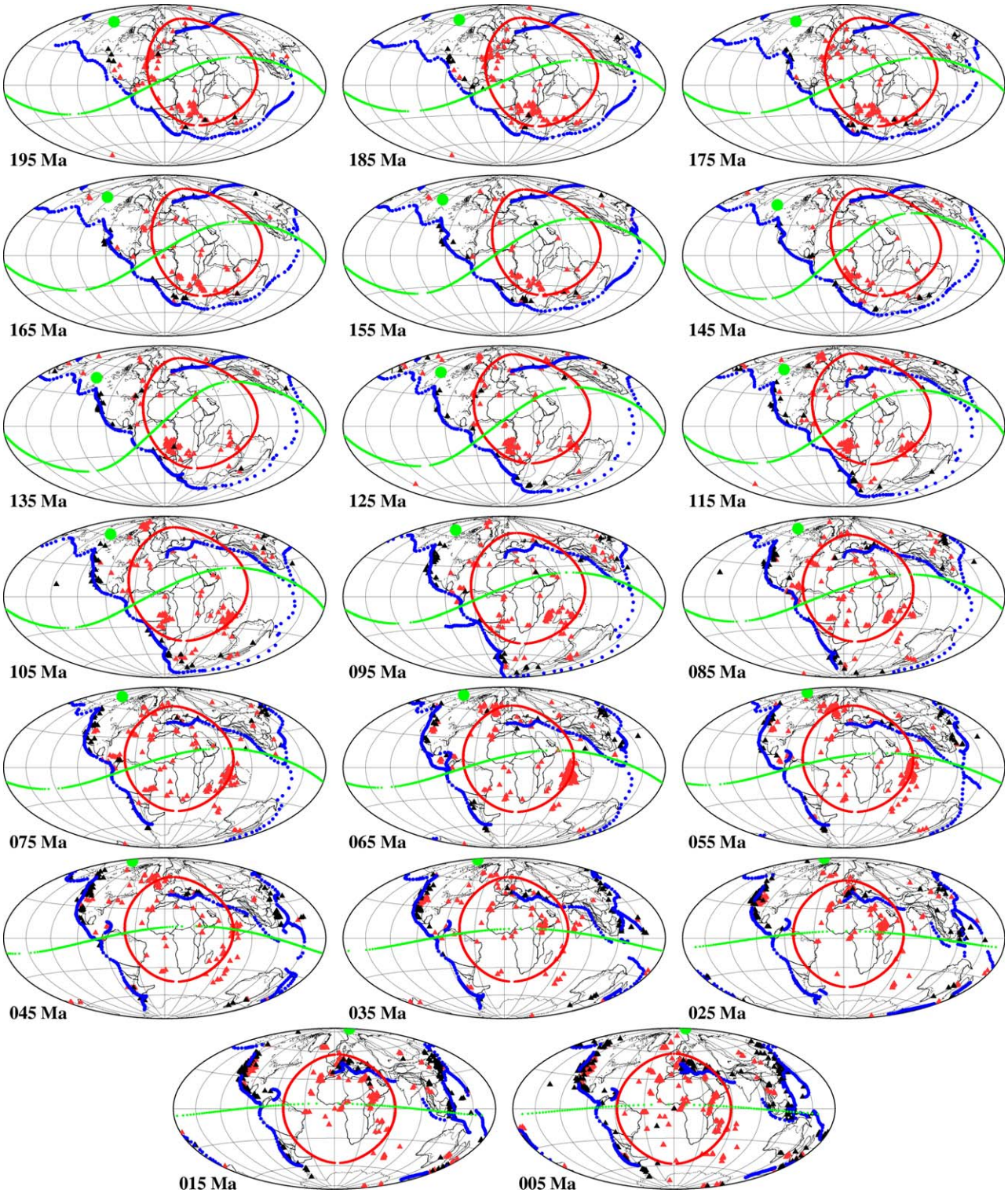

Figure B1. (continued)

B2. Upwelling

Mantle seismic tomographic models of shear velocity show two large-scale provinces in the lowermost part of the mantle with low velocities (Large Low Shear Velocity Provinces). They are thermochemical domes

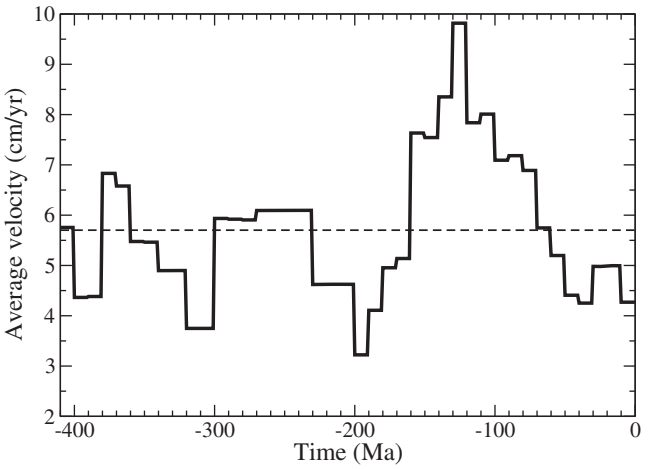

Figure B2. Average convergence velocity at Earth's surface: as a function of time (solid black line) and average value (dashed black line).

that may be chemically denser than the overlying mantle explaining its stability over long periods of time, but are probably overlain by hot and less dense large-scale upwellings which may dominate the effect on the geoid [*McNamara and Zhong*, 2005; *Steinberger and Torsvik*, 2012; *Ghosh et al.*, 2010]. These domes are associated with geoid highs such as the superswells currently observed at Earth's surface, beneath Africa and Polynesia [*Davaille*, 1999]. They are consequently modeled as regions with a negative mass anomalies with respect to the mantle. We arbitrarily fixed their density contrast with respect to the surrounding mantle to -50 kg/m^3, based on the conclusion of *Davaille* [1999] that doming regime should occur for density contrasts less than approximatively 1%, although these densities are still debated. These domes act as sources for many plumes swarms and models feature mantle plumes that are almost exclusively created at the margins of large thermochemical piles in the lowermost mantle [*Steinberger and Torsvik*, 2012]. Consequently, we assessed the center and width of the "African" dome from the small circles surrounding the intraplate alkaline volcanism at the surface. We found that the width of the small circle above the "African" dome has remained constant and about 45–50°, indicating that domes do not change size with time. The "Pacific" dome is assumed to have the same size and an antipodal position than the "African" dome.

We plot in Figure B1 the reconstructed intraplate volcanism (red triangle) for the past 410 Ma, in the fixed African plate reference frame as well as the small circle (in red) defining the area above the Africa dome. Note that the African dome remains close to a position being antipodal to the middle of the peri-Pacific ring of subduction, which is consistent with models showing that subduction history shapes lower mantle structure [*Bunge et al.*, 1998]. Tethyan-like subduction sometimes crosses the red circle contouring the African dome: this is currently observed in the tomography, where a region with fast shear velocity crosses the North/East part of the large low velocity zone at the bottom of the mantle.

The green point and the green great circle represent, respectively, the paleomagnetic pole and the associated paleomagnetic equator, in the fixed African plate reference frame [from *Torsvik et al.*, 2008]. For a better visualization of the positions of the domes, we rotate our fixed African plate reference frame toward the paleomagnetic reference frame, using the Euler poles of the Apparent

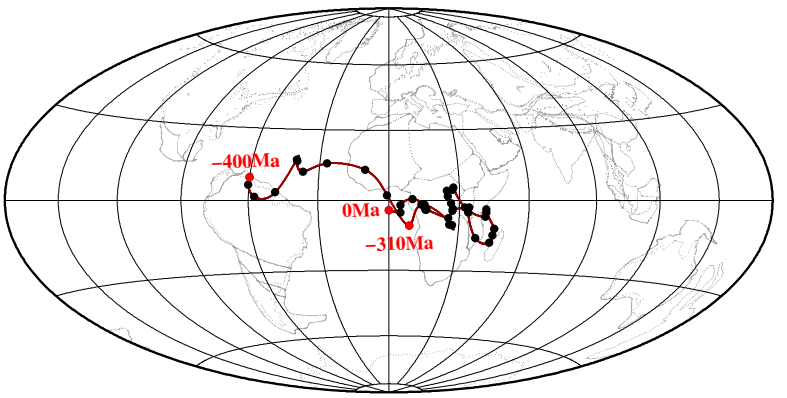

Figure B3. Location of the center of the African dome, for each 10 Myrs interval from −400Ma to present, in the paleomagnetic reference frame, superimposed to the present-day position of the continents (Hammer projection).

Wander Paths of Africa [*Torsvik et al*., 2008]: we plot on Figure B3 the center of the small circle as a function of time, superimposed to the present-day geography. Note that the African dome has remained close to the paleomagnetic equator, that is to say in a plane perpendicular to the rotation axis. The longitudinal drift along the equator is questionable because of the indetermination of any longitude by paleomagnetic methods. For the last 310 Myr, the dome has been under the present position of Africa.

Our model, only valid for long-wavelength mantle density heterogeneities, does not include returning passive upwelling from downwelling. The position of the domes does not arise naturally from the subduction history and their geometrical and physical parameters are set without taking into account the total mass conservation.

The aim of such a simple model is to perform sensitive experiments and even if it is difficult to reconcile with local observations, it explains present-day long-wavelength geoid, gravity and gravity gradients [*Panet et al*., 2014], as well as some features of True Polar Wander [*Rouby et al*., 2010; *Greff-Lefftz and Besse*, 2012].

Acknowledgments
We thank Nicolas Flament, Laurent Husson, and Christian Schiffer for their constructive reviews and their helpful comments on the original manuscript. Data related to the geodynamic model supporting the conclusions of this manuscript can be obtained in supporting information. This study is IPGP contribution 3868.

References

Alterman, Z., H. Jarosch, and C. H. Pekeris (1959), Oscillation of the Earth, *Proc. R. Soc. London Ser. A*, *252*, 80–95.
Bai, W., C. Vigny, Y. Ricard, and C. Froidevaux (1992), On the origin of deviatoric stresses in the lithosphere, *J. Geophys. Res.*, *97*, 11,729–11,737.
Balmer, M., P. E. Van Keken, and G. Ito (2015), Hotspots, large igneous provinces, and melting anomalies, in *Treatise on Geophysics*, 2nd ed., vol. 7, edited by G. Schubert, pp. 393–459, Elsevier, Oxford, U. K.
Becker, T. W., and L. Boschi (2002), A comparison of tomographic and geodynamic mantle models, *Geochem. Geophys. Geosyst.*, *3*(1), 1003, doi:10.129/2001GC000168.
Behn, M. D., C. P. Conrad, and P. G. Silver (2004), Detection of upper mantle flow associated with the African Superplume, *Earth Planet. Sci. Lett.*, *224*, 259–274.
Braun, J. (2010), The many surface expressions of mantle dynamics, *Nat. Geosci.*, *3*(12), 825–833, doi:10.1038/NGEO1020.
Braun, J., F. Guillocheau, C. Robin, G. Baby, and H. Jelsma (2014), Rapid erosion of the Southern African Plateau as it climbs over a mantle superswell, *J. Geophys. Res. Solid Earth*, *119*, 6093–6112, doi:10.1002/2014JB010998.
Bunge, H. P., M. A. Richards, C. Lithgow-Bertelloni, J. R. Baumgardner, S. P. Grand, and B. A. Romanowicz (1998), Time scales and heterogeneous structure in geodynamic earth models, *Science*, *280*(5360), 91–95.
Burke, K., and J. F. Dewey (1973), Plume-generated triple junctions: Key indicators in applying plate tectonics to old rocks, *J. Geol.*, *84*(4), 406–433.
Butterworth, N. P., A. S. Talsma, D. R. Müller, M. Seton, H. P. Bunge, B. S. A. Schuberth, G. E. Shephard, and C. Heine (2014), Geological, tomographic, kinematic and geodynamic constraints on the dynamics of sinking slabs, *J. Geodyn.*, *73*, 1–13.
Cande, S. C., and D. R. Stegman (2011), Indian and African plate motions driven by the push force of the Runion plume head, *Nature*, *475*, 47–52.
Chinnery, M. A. (1964), The strength of the Earth's crust under horizontal shear stress, *J. Geophys. Res.*, *69*, 2085–2089.
Cogné, J.-P., V. Kravchinsky, N. Halim, and F. Hankard (2005), Late Jurassic Early Cretaceous closure of the Mongol-Okhotsk Ocean demonstrated by new Mesozoic palaeomagnetic results from the Trans-Bakal area (SE Siberia), *Geophys. J. Int.*, *163*, 813–832, doi:10.1111/j.1365-246X.2005.02782.x.
Colli, L., S. Ghelichkhan, and H.-P. Bunge (2016), On the ratio of dynamic topography and gravity anomalies in a dynamic Earth, *Geophys. Res. Lett.*, *43*, 2510–2516, doi:10.1002/2016GL067929.
Coltice, N., B. R. Phillips, H. Bertrand, Y. Ricard, and P. Rey (2007), Global warming of the mantle at the origin of flood basalts over supercontinents, *Geology*, *35*(5), 391–394, doi:10.1130/G23240A.1.
Conrad, C. P. (2013), The solid Earth's influence on sea level, *Geol. Soc. Am. Bull.*, *125*(7/8), 1027–1052, doi:10.1130/B30764.1.
Conrad, C. P., and M. Gurnis (2003), Seismic tomography, surface uplift, and the breakup of Gondwanaland: Integrating mantle convection backwards in time, *Geochem. Geophys. Geosyst.*, *4*(3), 1031, doi:10.1029/2001GC000299.
Conrad, C. P., and L. Husson (2009), Influence of dynamic topography on sea level and its rate of change, *Lithosphere*, *1*(2), 110–120, doi:10.1130/L32.1.
Courtillot, V., A. Davaille, J. Besse, and J. Stock (2003), Three distinct types of hotspots in the Earth's mantle, *Earth Planet. Sci. Lett.*, *205*, 295–308.
Curray, J. R., and T. Munasinghe (1991), Origin of the Rajmahal Traps and the 85E Ridge: Preliminary reconstructions of the trace of the Crozet hotspot, *Geology*, *19*, 1237–1240.
Czarnota, K., G. G. Roberts, N. J. White, and S. Fishwick (2014), Spatial and temporal patterns of Australian dynamic topography from River Profile Modeling, *J. Geophys. Res. Solid Earth*, *119*, 1384–1424, doi:10.1002/2013JB010436.
Dahlen, F. A., and J. Tromp (1998), *Theoretical Global Seismology*, Princeton Univ. Press, N. J.
Davaille, A. (1999), Simultaneous generation of hotspots and superswells by convection in a heterogeneous planetary mantle, *Nature*, *402*(6763), 756–760, doi:10.1038/45461.
Davaille, A., E. Stutzmann, G. Silveira, J. Besse, and V. Courillot (2005), Convective patterns under the Indo-Atlantic box, *Earth Planet. Sci. Lett.*, *239*, 233–252.
Domeier, M., and T. Torsvik (2014), Plate tectonics in the late Paleozoic, *Geosci. Front.*, *5*, 303–350.
Domeier, M., P. V. Doubrovine, T. H. Torsvik, W. Spakman, and A. L. Bull (2016), Global correlation of lower mantle structure and past subduction, *Geophys. Res. Lett.*, *43*, 4945–4953, doi:10.1002/2016GL068827.
Flament, N., M. Gurnis, and D. Müller (2013), A review of observations and models of dynamic topography, *Lithosphere*, *5*(2), 189–210, doi:10.1130/L245.1.

Flament, N., M. Gurnis, S. Williams, M. Seton, J. Skogseid, C. Heine, and R. D. Müller (2014), Topographic asymmetry of the South Atlantic from global models of mantle flow and lithospheric stretching, *Earth Planet. Sci. Lett.*, *387*, 107–119.
Flament, N., M. Gurnis, D. Müller, D. Bower, and L. Husson (2015), Influence of subduction history on South American topography, *Earth Planet. Sci. Lett.*, *430*, 9–18.
Fleitout, L., and C. Froidevaux (1982), Tectonics and topography for a lithosphere containing densities heterogeneities, *Tectonics*, *1*, 21–56.
Fleitout, L., and C. Froidevaux (1983), Tectonic stresses in the lithosphere, *Tectonics*, *2*, 315–324.
Flowers, R. M., and B. Schoene (2010), (UTh)/He thermochronometry constraints on unroofing of the eastern Kaapvaal craton and significance for uplift of the southern African Plateau, *Geology*, *38*, 827–830.
Frizon de Lamotte, D., B. Fourdan, S. Leleu, F. Leparmentier, and P. de Clarens (2015), Style of rifting and the stages of Pangea breakup, *Tectonics*, *34*, 1009–1029, doi:10.1002/2014TC003760.
Fukao, Y., S. Widiyantoro, and M. Obayashi (2001), Stagnant slabs in the upper and lower mantle transition region, *Rev. Geophys.*, *39*, 291–323.
Ghosh, A., W. E. Holt, A. J. Haines, and L. M. Flesch (2006), Gravitational potential energy of the Tibetan Plateau and the forces driving the Indian plate, *Geology*, *34*, 321–324.
Ghosh, A., W. E. Holt, L. Wen, A. J. Haines, and L. M. Flesch (2008), Joint modeling of lithosphere and mantle dynamics elucidating lithosphere-mantle coupling, *Geophys. Res. Lett.*, *35*, L16309, doi:10.1029/2008GL034365.
Ghosh, A., T. W. Becker, and S. Zhong (2010), Effects of lateral viscosity variations on the geoid, *Geophys. Res. Lett.*, *37*, L01301, doi:10.1029/2009GL040426.
Ghosh, A., W. E. Holt, and L. Wen (2013), Predicting the lithospheric stress field and plate motions by joint modeling of lithosphere and mantle dynamics, *J. Geophys. Res. Solid Earth*, *118*, 346–368, doi:10.1029/2012JB009516.
Gibbons, A. D., J. M. Whittaker, and R. D. Müller (2013), The breakup of East Gondwana: Assimilating constraints from Cretaceous ocean basins around India into a best-fit tectonic model, *J. Geophys. Res. Solid Earth*, *118*, 808–822, doi:10.1002/jgrb.50079.
Greff-Lefftz, M., and J. Besse (2012), Paleo movement of continents since 300 Ma, mantle dynamics and large wander of the rotational pole, *Earth Planet. Sci. Lett.*, *345*, 151–158.
Greff-Lefftz, M., L. Métivier, and J. Besse (2010), Dynamic mantle density heterogeneities and global geodetic observables, *Geophys. J. Int.*, *180*(3), 1080–1094, doi:10.1111/j.1365-246X.2009.04490.x.
Guillaume, B., S. Pochat, J. Monteux, L. Husson, and G. Choblet (2016), Can eustatic charts go beyond first order? Insights from the Permian-Triassic, *Lithosphere*, *8*(5), 505–518.
Guiraud, R., and J.-C. Maurin (1992), Early Cretaceous rifts of Western and Central Africa: An overview, in Geodynamics of Rifting, vol. II: Case History Studies on Rifts: North and South America and Africa, edited by P. A. Ziegler, Tectonophysics, *213*, 153–168.
Guiraud, R., W. Bosworth, J. Thierry, and A. Delplanque (2005), Phanerozoic geological evolution of Northern and Central Africa: An overview, *J. Afri. Earth Sci.*, *43*, 83–143.
Gurnis, M. (1990), Bounds on global dynamic topography from Phanerozoic flooding of continental platforms. *Nature*, *344*(6268), 754–756, doi:10.1038/344754a0.
Gurnis, M. (1993), Phanerozoic marine inundation of continents driven by dynamic topography above subducting slabs, *Nature*, *364*, 589–593, doi:10.1038/364589a0.
Gurnis, M., R. D. Müller, and L. Moresi (1998), Cretaceous vertical motion of Australia and the Australian Antarctic Discordance, *Science*, *279*(5356), 1499–1504, doi:10.1126/science.279.5356.1499.
Gvirtzman, Z., C. Faccenna, and T. W. Becker (2016), Isostasy, flexure, and dynamic topography, *Tectonophysics*, *683*, 255–271.
Haq, B. U., J. Hardenbol, and P. R. Vail (1987), Chronology of fluctuating sea levels since the Triassic, *Science*, *235*, 1156–1167.
Haq, B. U., and A. M. Al-Qahtani (2005), Phanerozoic cycles of sea-level change on the Arabian Platform, *GeoArabia*, *10*(2), 127–160.
Heine, C., R. D. Muller, B. Steinberger, and L. DiCaprio (2010), Integrating deep Earth dynamics in paleogeographic reconstructions of Australia, *Tectonophysics*, *483*(1–2), 135–150.
Hoggard, M. J., N. White, and D. Al-Attar (2016), Global dynamic topography observations reveal limited influence of large-scale mantle flow, *Nat. Geosci.*, *9*, 456–463.
Lithgow-Bertelloni, C., and M. Gurnis (1997), Cenozoic subsidence and uplift of continents from time-varying dynamic topography, *Geology*, *2*(8), 735–738, doi:10.1130/0091-7613.
Lithgow-Bertelloni, C., and J. H. Guynn (2004), Origin of the lithospheric stress field, *J. Geophys. Res.*, *109*, B01408, doi:10.1029/2003JB002467.
Lithgow-Bertelloni, C., and M. A. Richards (1998), The dynamics of cenozoic and mesozoic plate motions, *Rev. Geophys. 36*, 27–78.
Lithgow-Bertelloni, C., and P. G. Silver (1998), Dynamic topography, plate driving forces and the African superswell, *Nature*, *395*(6699), 269–272, doi:10.1038/26212.
Liu, L. (2015), The ups and downs of North America: Evaluating the role of mantle dynamic topography since the Mesozoic, *Rev. Geophys.*, *53*, 1022–1049, doi:10.1002/2015RG000489.
Liu, L., and M. Gurnis (2010), Dynamic subsidence and uplift of the Colorado Plateau, *Geology*, *38*(7), 663–666.
Liu, L., S. Spasojevic, and M. Gurnis (2008), Reconstructing Farallon plate subduction beneath North America back to the Late Cretaceous, *Science*, *322*(5903), 934–938, doi:10.1126/science.1162921.
Liu, S., D. Nummedal, and L. Liu (2011), Migration of dynamic subsidence across the Late Cretaceous United States Western Interior Basin in response to Farallon plate subduction, *Geology*, *39*(6), 555–558, doi:10.1130/G31692.1.
McKenzie, D. (1978), Some remarks on the development of sedimentary basins, *Earth Planet. Sci. Lett.*, *40*(1), 25–32.
McNamara, A., and S. Zhong (2005), Thermochemical structures beneath Africa and the Pacific Ocean, *Nature*, *437*, 1136–1139, doi:10.1038/nature04066.
Matthews, K. J., A. J. Hale, M. Gurnis, R. D. Muller, and L. DiCaprio (2011), Dynamic subsidence of Eastern Australia during the Cretaceous, *Gondwana Res*, *19*(2), 372–383, doi:10.1016/j.gr.2010.06.006.
Matthews, K. J., K. T. Maloney, S. Zahirovic, S. E. Williams, M. Seton, and R. D. Mller (2016), Global plate boundary evolution and kinematics since the late Paleozoic, *Global Planet. Change*, *146*, 226–250, doi:10.1016/j.gloplacha.2016.10.002.
Mitrovica, J. X., and G. T. Jarvis (1985), Surface deflections due to transient subduction in a convecting mantle, *Tectonophysics*, *120*, 211–237, doi:10.1016/0040-1951(85) 90052–6.
Mitrovica, J. X., C. Beaumont, and G. T. Jarvis (1989), Tilting of continental interiors by the dynamical effects of subduction, *Tectonics*, *8*, 1079–1094, doi:10.1029/TC008i005p01079.
Molnar, P., P. C. England, and C. H. Jones (2015), Mantle dynamics, isostasy, and the support of high terrain, *J. Geophys. Res. Solid Earth*, *120*, 1932–1957, doi:10.1002/2014JB011724.
Moucha, R., and A. Forte (2011), Changes in African topography driven by mantle convection, *Nat. Geosci.*, *4*(10), 707–712, doi:10.1038/ngeo1235.

Moucha, R., A. M. Forte, D. B. Rowley, J. X. Mitrovica, N. A. Simmons, and S. P. Grand (2008), Mantle convection and the recent evolution of the Colorado Plateau and the Rio Grande Rift valley, *Geology*, *36*, 439–442.
Moucha, R., A. Forte, D. Rowley, J. X. Mitrovica, N. A. Simmons, and S. P. Grand (2009), Deep mantle forces and the uplift of the Colorado Plateau, *Geophys. Res. Lett*, *36*, L19310, doi:10.1029/2009GL039778.
Müller, R. D et al. (2016), Ocean basin evolution and global-scale plate reorganization events since Pangea breakup, *Annu. Rev. Earth Planet. Sci.*, *44*, 107–138.
Panet, I., G. Pajot-Métivier, M. Greff-Lefftz, L. Métivier, M. Diament, and M. Mandea (2014), Mapping the mass distribution of Earths mantle using satellite-derived gravity gradients, *Nat. Geosci.*, *7*, 131–135, doi:10.1038/ngeo2063.
Peltier, W. R. (1974), Impulse response of a Maxwell Earth, *Rev. Geophys. Space Phys.*, *12*, 649–669.
Reeves, C. (2014), The position of Madagascar within Gondwana and its movements during Gondwana dispersal, *J. Afr. Earth Sci.*, *94*, 45–57, doi:10.1016/j.jafrearsci.2013.07.011.
Ren, Y., E. Stutzmann, R. D. van der Hilst, and J. Besse (2007), Understanding seismic heterogeneities in the lower mantle beneath the Americas from seismic tomography and plate tectonic history, *J. Geophys. Res.*, *112*, B01302, doi:10.1029/2005JB004154.
Ricard, Y., L. Fleitout, and C. Froidevaux (1984), Geoid heights and lithospheric stresses for a dynamic Earth, *Ann. Geophys.*, *2*, 267–286.
Ricard, Y., M. Richards, C. Lithgow-Bertelloni, and Y. LeStunff (1993), A geodynamic model of mantle density heterogeneity, *J. Geophys. Res. 98*, 21,895–21,909.
Ricard, Y., E. Mattern, and J. Matas (2005), Mineral physics in thermo-chemical mantle models, *Composition, Structure and Evolution of the Earth Mantle*, *AGU Monogr.*, vol. 160, edited by R. Hilst et al., pp. 283–300, Washington, D. C.
Richards, M. A., and B. Hager (1984), Geoid anomalies in a dynamic Earth, *J. Geophys. Res. 89*, 5987–6002.
Rouby, H., M. Greff-Lefftz, and J. Besse (2010), Mantle dynamics, geoid, inertia and TPW since 120 Ma, *Earth Planet. Sci. Lett.*, *292*(3–4), 301–311.
Rudge, J. F., G. G. Roberts, N. J. White, and C. N. Richardson (2015), Uplift histories of Africa and Australia from linear inverse modeling of drainage inventories, *J. Geophys. Res. Earth Surface*, *120*, 894–914, doi:10.1002/2014JF003297.
Schettino, A., and C. R. Scotese (2005), Apparent polar wander paths for the major continents (200 Ma to the present-day): A palaeomagnetic reference frame for global plate tectonic reconstructions, *Geophys. J. Int.*, *163*(2), 727–759, doi:10.1111/j.1365-246X.2005.02638.x.
Schiffer, C., and S. B. Nielsen (2016), Implications for anomalous mantle pressure and dynamic topography from lithospheric stress patterns in the North Atlantic Realm, *J. Geodyn.*, *98*, 53–69, doi:10.1016/j.jog.2016.03.014.
Ségoufin, J., and P. Patriat (1980), Existence d'anomalies mesozoiques dans le bassin de Mozambique, *C. R. Acad. Sci.*, *287*, 109–112.
Seton, M., et al. (2012), Global continental and ocean basin reconstructions since 200 Ma, *Earth Sci. Rev.*, *113*, 212–270.
Spasojević, S., and M. Gurnis (2012), Sea level and vertical motion of continents from dynamic Earth models since the Late Cretaceous, *AAPG Bull.*, *96*(11), 2037–2064, doi:10.1306/03261211121.
Spasojević, S., L. Liu, and M. Gurnis (2009), Adjoint models of mantle convection with seismic, plate motion, and stratigraphic constraints: North America since the Late Cretaceous, *Geochem. Geophys. Geosyst.*, *10*, Q05W02, doi:10.1029/2008GC002345.
Steinberger, B. (2016), Topography caused by mantle density variations: Observation-based estimates and models derived from tomography and lithosphere thickness, *Geophys. J. Int.*, *205*, 604–621.
Steinberger, B., and T. H. Torsvik (2012), A geodynamic model of plumes from the margins of Large Low Shear Velocity Provinces, *Geochem. Geophys. Geosyst.*, *13*, Q01W09, doi:10.1029/2011GC003808.
Steinberger, B., H. Schmeling, and G. Marquart (2001), Large-scale lithospheric stress field and topography induced by global mantle circulation, *Earth Planet. Sci. Lett.*, *186*, 75–91.
Steinberger, B., T. H. Torsvik, and T. W. Becker (2012), Subduction to the lower mantle a comparison between geodynamic and tomographic models, *Solid Earth*, *3*, 415–432, doi:10.5194/se-3-415-2012.
Storey, M., J. J. Mahoney, A. D. Saunders, R. A. Duncan, S. P. Kelley, and M. F. Coffin (1995), Timing of hot spot-related volcanism and the break-up of Madagascar and India, *Science*, *267*, 852–855.
Struckmeyer, H. I. M., and P. J. Brown (1990), Australian sea level curves: Part 1. Australian inundation curves, BMR J. Aust. Geol. Geophys., 1990/11, 67 pp.
Torsvik, T. H., R. D. Tucker, L. D. Ashwal, E. A. Eide, N. A. Rakotosolofo, and M. J. de Wit (1998), Late Cretaceous magmatism in Madagascar: Palaeomagnetic evidence for a stationary Marion hotspot, *Earth Planet. Sci. Lett.*, *164*, 221–232.
Torsvik, T. H., R. D. Mueller, R. Van der Voo, S. Steinberger, and C. Gaina (2008), Global plate motion frames: Toward a unified model, *Rev. Geophys.*, *46*, RG3004, doi:10.1029/2007RG000227.
Van der Meer, D. G., W. Spakman, D. J. J. van Hinsbergen, M. Amaru, and T. H. Torsvik (2010), Towards absolute plate motions constrained by lower-mantle slab remnants, *Nat. Geosci.*, *3*, 36–40.
Wang, X., W. E. Holt, and A. Ghosh (2015), Joint modeling of lithosphere and mantle dynamics: Evaluation of constraints from global tomography models, *J. Geophys. Res. Solid Earth*, *120*, 8633–8655, doi:10.1002/2015JB012188.
Yang, T., and M. Gurnis (2016), Dynamic topography, gravity and the role of lateral viscosity variations from inversion of global mantle flow, *Geophys. J. Int.*, *207*, 1186–1202.
Zhang, N., S. Zhong, and R. M. Flowers (2012), Predicting and testing continental vertical motion histories since the Paleozoic, *Earth Planet. Sci. Lett.*, *317–318*, 426–435.